Assembly and Characterization of a High Numerical Aperture Microscope for Single Atoms

Masterarbeit im Studiengang MSc. Physik
von

Felix Kleißler

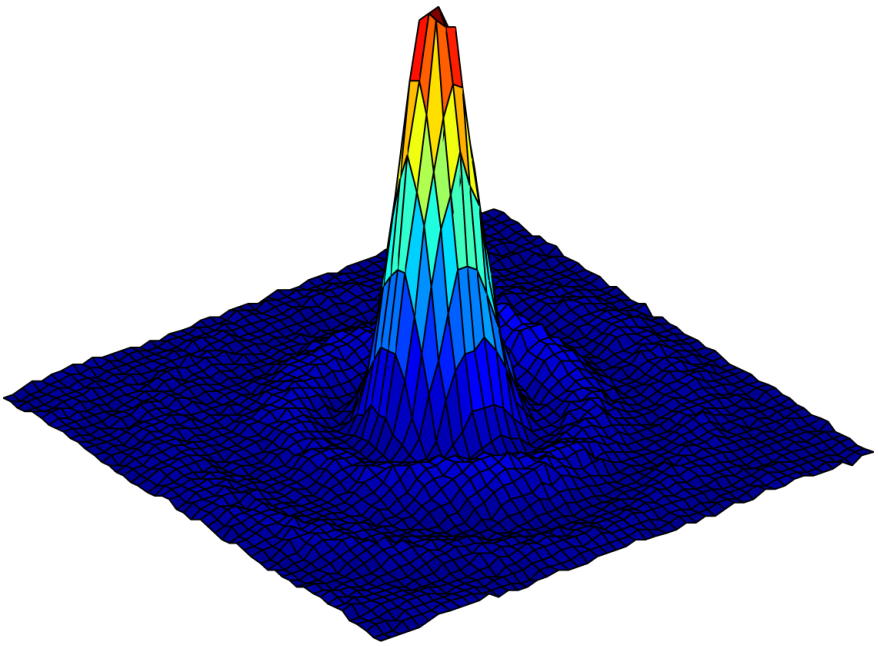

angefertigt im
INSTITUT FÜR ANGEWANDTE PHYSIK
vorgelegt der
MATHEMATISCH-NATURWISSENSCHAFTLICHEN FAKULTÄT
der
RHEINISCHEN FRIEDRICH-WILHELMS-UNIVERSITÄT BONN

August 2014

1. Gutachter: Prof. Dr. Dieter Meschede

2. Gutachter: Prof. Dr. Martin Weitz

This master thesis investigates the optical imaging properties of a state of the art in-house developed objective for the observation of single atoms trapped in a two-dimensional spin-dependent optical lattice. After the successful assembly of the objective lenses into a ceramic holder two different approaches for the characterization are presented. First a wave-front analysis for the estimation of the root-mean-square deviation to a planar reference using a Shack-Hartmann sensor and a Shearing interferometer is performed. In the second approach the imaging of a point-like light-source is utilized to determine the point-spread-function of the objective. The production of the probes is inspired by methods of optical microscopy in the nano-scale regime like Total-Internal-Reflexion-Fluorescence- and Scanning-Nearfield-Optical-Microscopy. Self-written `MATLAB`-routines are used to extract quantitative information on the imaging system. The analysis in this work shows that the objective can operate close to diffraction limit with a numerical aperture of 0.9. Numerically calculated point-spread-functions are compared to the measurements to explain the small deviations to the perfect Airy pattern. A very good agreement has been found between the point-spread-function calculated numerically and that measured in the characterization set-up.

Contents

1. Introduction **7**

2. Imaging Theory **9**

2.1. Diffraction Theory 9

2.1.1. Diffraction by an arbitrary aperture 9

2.1.2. Diffraction by a lens 11

2.2. Point Spread Function 12

2.3. Optical Transfer Function 14

2.4. Ray tracing 16

2.5. Optical Path Difference 16

2.6. Imaging with a high Numerical Aperture Objective 16

2.6.1. Apodization 17

2.6.2. Depolarization 17

2.6.3. Aberrations and Strehl intensity 18

2.7. Summary 19

3. In-house developed microscope for single atoms **21**

3.1. Physical properties 21

3.2. Assembly under clean-room condition 23

4. Characterization Setup **25**

4.1. Wavefront analysis 25

4.1.1. Shear-plate-interferometer analysis 26

4.1.2. Shack-Hartmann wavefront sensor 27

4.2. Measuring of the Point-Spread-Function 28

4.2.1. Pinhole approach 28

4.2.2. Imaging of Nano-particles 29

4.2.3. Imaging of a SNOM-fiber tip 30

4.3. Comparison of the measurement methods 31

5. Analysis Software **35**

5.1. OSLO-Software 35

5.1.1. Scan through focus 36

5.2. MATLAB-Software 38

5.2.1. Data processing 38

5.2.2. Calculation of the numerical aperture and Strehl ratio 39

5.2.3. Calculation of the Modulation Transfer Function 40
5.2.4. Application on modeled detector Signal 41
5.2.5. Defocussing Analysis 42

6. Characterization of a high NA Objective **45**
6.1. Numerical aperture and Strehl intensity 45
6.2. Modulation Transfer Function 46
6.3. Spherical aberration analysis 47
6.4. NA in dependence of the Aperture 48

7. Summary and Outlook **51**

A. Construction of a sub-micrometer scale light Source **53**
A.1. SNOM-fiber preparation 53
A.2. Production of pinholes 54

Acknowledgments **55**

Bibliography **57**

Declaration **61**

1. Introduction

In 1982 Feynman introduced the concept of quantum simulator - a device which can simulate the behavior of quantum systems that cannot otherwise be computed with classical resources [1]. It was shown that the required memory space and computational time increases exponential with the number of quantum variables in a classical computer [2]. Feynman suggested to use a quantum mechanical system to simulate the behavior of another one. The general idea is to prepare an initial state, receive a final state after evolution of the system and finally measure a quantity of interest [3]. Today quantum simulators are realized to some extend for example photonic quantum simulators [4] and super conducting on-chip systems [5].

Furthermore within the last decades experimental advances in the observation and coherent manipulation of atoms paved the way for the simulation of quantum mechanical effects using ultra cold atoms trapped in optical lattices [6]. In this kind of system atoms are prepared in a well defined initial position and spin state. Afterwards an experimental sequence is applied to the quantum mechanical system or it develops freely. At the end of each sequence the final state of the quantity of interest has to be determined by fluorescence imaging.

For most of the experiments using single ultra cold atoms in optical lattices the quantity of interest is the spatial distribution of the atoms. For the observation of initial and final state a high quality imaging system is needed since the lattice constant of an optical lattice [7] is in the order of several hundred nanometer. The minimal resolvable distance is anti-proportional to the numerical aperture (NA) of a diffraction limited imaging system. Hence a high NA is desired to determine the position of atoms with single lattice site resolution. If the resolution of a system is not sufficient to observe with single lattice site resolution complicated algorithms (e.g. [8, 9]) have to be used.

Another feature of a diffraction limited high numerical aperture microscope for single atoms is the possibility to address atoms with single lattice site resolution. This technique is much more convenient than e.g. magnetic resonance technique presented in [11]. Since each optical path is invertible a microscope can be used to focus down a laser beam and address single atoms. Consider an atom with the two hyperfine states $|1\rangle$, $|2\rangle$ and a microwave field which is red-detuned to their transition energy (Fig.1.1.b)). An addressing beam impinging on a single lattice site locally induces a differential light shift Δ_{LS} in the sense that it displaces the distance between the two qubit energy levels. Under the right conditions the differential light shift tunes the atom into resonance with the microwave field [10]. Therefore the spin is flipped by the microwave field deterministically at exactly one lattice site. The described method is a powerful tool for the preparation of the initial system of an experimental sequence.

In the Institute of Applied Physics (IAP) in Bonn a new two-dimensional discrete quantum simulator is under construction. The apparatus is designed to achieve a diffraction limited mi-

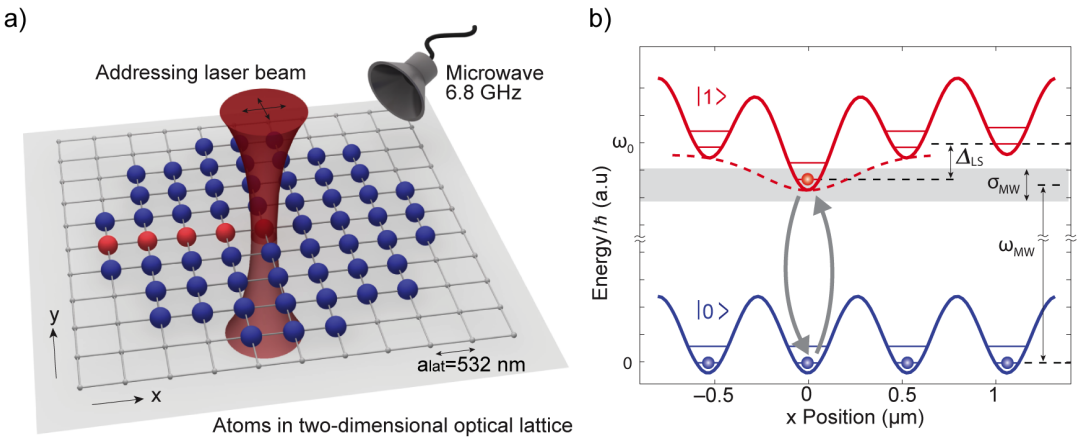

Figure 1.1.: a) Atoms with in a two dimensional optical lattice. A focused laser beam performs the single site addressing and the microwave source flips the spin. b) Energy diagram of an atom with the hyperfine states $|1\rangle$ and $|2\rangle$. The microwave field ω_{MW} is red-detuned to the transition. At position $x = 0$ the addressing beam induces the light-shift Δ_{LS} and tunes the energy level in resonance with the microwave field. [10]

croscope with a numerical aperture NA above 0.9. To our best knowledge the largest numerical aperture quantum gas microscope features at present NA ~ 0.8 (Harward, [12]). Moreover the experiment features a two-dimensional spin dependent optical lattice with a lattice constant of $a \approx 612\,\text{nm}$ based on the technique presented in [13]. The lattice will be placed in the focal plane of the microscope for the observation of single atoms. Hence the apparatus will allow the control of neutral atoms with outstanding precision.

In this thesis a detailed characterization of the quantum gas microscope will be presented. All tests were performed outside the vacuum system by imaging nano-objects, though not yet single atoms. Nevertheless in the text it will often be referred to as microscope for single atoms since the imaging performance is expected to be similar in the later experiment. It will be proved that the objective is working close to the diffraction limited regime and that the resolution is as expected. Moreover the dependence of the NA from the free aperture is determined. All measured values are compared to the modeled one calculated by a simulation software.

2. Imaging Theory

In the following the theoretical aspects needed for the understanding of this thesis will be introduced. First diffraction theory will be discussed on the basis of simple examples. The limitations on the resolution due to diffraction and the formula of the Airy pattern will be derived. The conversion of the spatial intensity distribution into spatial frequency space is described by the optical transfer function. Ray tracing as a method to design and evaluate optical systems will be discussed shortly. Furthermore wavefronts and optical path difference for the description of the quality of an optical system are introduced. Finally the features of a high numerical aperture imaging system are discussed briefly.

2.1. Diffraction Theory

In this section the most important formulas for imaging of a point-source based on diffraction are introduced. For simplicity and to give an intuitive picture the intensity distribution in the image plane of a thin lens under the paraxial approximation is derived.

Huygens and Fresnel introduced the principle of diffraction to describe the propagation of light after hitting an obstacle. It was observed that the propagation strongly diverges from the predictions of geometrical optics. The principle includes the following assumptions [14]:

- Each point of a wavefront is the initial point of a secondary spherical wave
- The wavefront at a later time can be described by the envelope of all spherical waves
- Speed and frequency of the secondary waves are the same as of the primary wave
- The amplitude at a point is given as the superposition of the secondary waves

In Sec.2.1.1 and Sec.2.1.2 this assumptions will be used to derive the electric field of a monochromatic wave after passing an arbitrary aperture and a circular lens respectively.

2.1.1. Diffraction by an arbitrary aperture

To describe the diffraction of a monochromatic wave due to an arbitrary aperture a simple picture based on the assumptions introduced in Sec.2.1 is introduced. In Fig.2.1 the used coordinate system with all relevant quantities is presented.

In the diffraction plane (aperture plane) at each position $P(x_1, y_1)$ within the aperture a secondary spherical wave is emitted which is observed at position $P(x_2, y_2)$ in the imaging plane. In general the field of a spherical wave with amplitude unity can be expressed by $A(r) = \exp(-ikr)/r$, where r is the distance between source and observation point. The

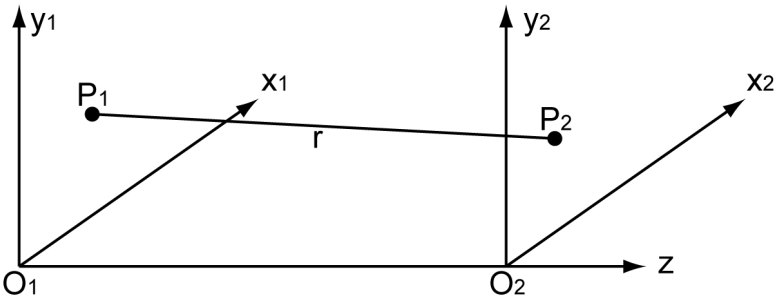

Figure 2.1.: Sketch of the coordinate system. O_1 is the diffraction plane and O_2 the observation plane. A spherical wave originating at P_1 is observed in a distance r at point P_2.

amplitude of the secondary wave depends on the incoming field and hence on the position on the aperture. It is described by the term $A_1(x_1, y_1)$. To obtain the field at any position $A_2(x_2, y_2)$ one has to calculate the superposition over all secondary waves, which is equivalent to the integral over the diffraction plane.

$$A_2(x_2, y_2) = \frac{i}{\lambda} \int \int_{-\infty}^{\infty} A_1(x_1, y_1) \frac{\exp(-ikr(x_1, y_1))}{r(x_1, y_1)} dx_1 dy_1 \tag{2.1}$$

The pre-factor $\frac{i}{\lambda}$ has its origin in the explicit derivation of Eq.2.1 out of Maxwell's equations using the Greens theorem (see [14, 15]). For geometric reasons the distance r between the points P_1 and P_2 is expressed by.

$$r^2 = z^2 + (x_2 - x_1)^2 + (y_2 - y_1)^2 = z^2 \left[1 + \frac{(x_2 - x_1)^2 + (y_2 - y_1)^2}{z^2} \right] \tag{2.2}$$

This expression simplifies under the assumption that the observation point P_2 is not far away from the optical axis ($(x_2 - x_1)^2 + (y_2 - y_1)^2 \ll z^2$) to:

$$r \approx z \left[1 + \frac{(x_2 - x_1)^2 + (y_2 - y_1)^2}{2z^2} \right] \tag{2.3}$$

Using the obtained term for r in Eq.2.1 yields:

$$\begin{aligned} A_2(x_2, y_2) \quad = \quad & \frac{i \exp(-ikz)}{\lambda z} \int \int_{\infty}^{-\infty} A_1(x_1, y_1) \times \\ & \exp \left\{ -\frac{ik}{2z} \left[(x_2 - x_1)^2 + (y_2 - y_1)^2 \right] \right\} dx_1 dy_1 \end{aligned} \tag{2.4}$$

The first exponential term corresponds to the phase gained by a wave traveling the distance z. And the exponential term in the integral corresponds to the phase gained by the displacement between P_1 and P_2.

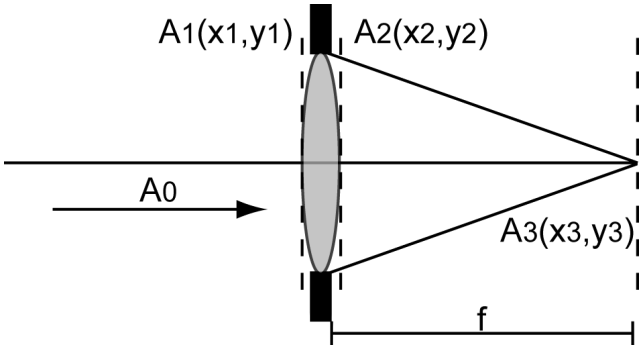

Figure 2.2.: A planar wavefront with amplitude A_0 approaches the lens from the left hand side and creates the field A_1 in the plane in front of the lens. The amplitude and phase are changed by the lens medium and the field is changed to A_2. In the image plane the field A_3 is observed.

2.1.2. Diffraction by a lens

On the basis of Eq.2.4 for an incoming planar wave the field in the focus of a lens can be calculated since every lens has an aperture of finite size. A sketch of the assumed situation is shown in Fig.2.2. In the formula of the field some additional terms appear due to the refractive index of the lens medium. During the transmission through the lens the field gains an additional phase in dependence of the lens thickness at each position. Furthermore according to the Fresnel equation [16] the transmitted amplitude depends on the incidence angle and hence on the position. The transmission of a lens with spherical surfaces can be expressed as [14]:

$$t(x,y) = P(x,y)\exp\left[\frac{ik(x^2+y^2)}{2f}\right] \tag{2.5}$$

Here $P(x,y)$ is the pupil function and describes the change of the amplitude. Inserting $t(x,y)$ into Eq.2.4 and calculating the exponential terms explicitly delivers:

$$\begin{aligned} A_3(x_3,y_3) &= \frac{iA_0}{\lambda f}\exp(-ikf)\exp\left[-\frac{ik}{2f}(x_3^2+y_3^2)\right]\times \\ &\quad \int\int_{-\infty}^{\infty} P(x_2,y_2)\exp\left[\frac{ik}{f}(x_3x_2+y_3y_2)\right]dx_2dy_2 \end{aligned} \tag{2.6}$$

Here A_0 is the amplitude of the incoming planar wave. The integral in the second row of Eq.2.6 can be interpreted as the two dimensional Fourier transformation of the pupil function $P(x,y)$.

$$F(x_2,y_2) = \int\int P(x_2,y_2)\exp\left[\frac{ik}{f}\left(x_3x_2+y_3y_2\right)\right]dx_2dy_2 \tag{2.7}$$

By defining the frequencies $n = x_3/(\lambda f)$ and $m = y_3/(\lambda f)$ and using the polar coordinates $x = r\cos\Phi$, $y = r\sin\Phi$ and $m = l\cos\Psi$, $n = l\sin\Psi$ the Fourier transformation can be expressed as:

$$F(l,\Psi) = \int_0^\infty \int_0^{2\pi} P(r,\Phi)\exp\left(-i2\pi rl\cos(\Phi-\Psi)\right) r dr d\Phi \tag{2.8}$$

For a circular symmetric lens without loss of generality the angle Ψ can be fixed to $\Psi = 0$. Hence Eq.2.8 can be expressed by:

$$F(l) = \int_0^\infty 2\pi r P(r) J_0(krl) dr \tag{2.9}$$

Where the integral representation of the Bessel function of kind one and order zero ($J_0(x) = \frac{1}{2\pi}\int_0^{2\pi}\exp(-ix\cos(\tau))d\tau$) was used. Assuming the pupil function is unity for $r \leq a$ and zero for $r > a$, where a is the radius of the aperture, one obtains:

$$F(l) = \pi a^2 \frac{2J_1\left(\frac{2\pi al}{\lambda f}\right)}{\left(\frac{2\pi al}{\lambda f}\right)} \tag{2.10}$$

Here the identity $\int_0^x x_0 J_0(x_0)dx_0 = xJ_1(x)$ was used. Inserting this expression in Eq.2.6 yields an equation for the field in the focus plane of a circular lens:

$$A_3(r_3) = \frac{i\pi a^2}{\lambda f}\exp(-ikf)\exp\left(-\frac{i\pi r_3^2}{\lambda f}\right)\left[\frac{2J_1\left(\frac{2\pi r_3 a}{\lambda f}\right)}{\left(\frac{2\pi r_3 a}{\lambda f}\right)}\right] \tag{2.11}$$

Where $r_3 = \sqrt{x_3^2 + y_3^2}$ is the radial distance in the image plane. A point can not be imaged into a single spot since the field is a function of r_3. Therefore the resolution is limited by diffraction. The equation of the intensity is the modulus squared of Eq.2.11 and called the Airy disk.

2.2. Point Spread Function

Point Spread Functions (PSF) describe how an idealized point-source is imaged by an optical system. The observed image is the intensity distribution within the focal plane. Hence the PSF of an ideal circular lens is obtained by calculating the modulus squared of the field described by Eq.2.11. To simplify the expression some quantities are introduced. First the numerical aperture (NA) is defined by:

$$\text{NA} = n\sin\alpha \approx n\frac{a}{f} \tag{2.12}$$

Where n is the refractive index of the medium between the lens and the object. Since in most cases the medium between the lenses is air the refractive index $n = 1$ and the NA is a pure

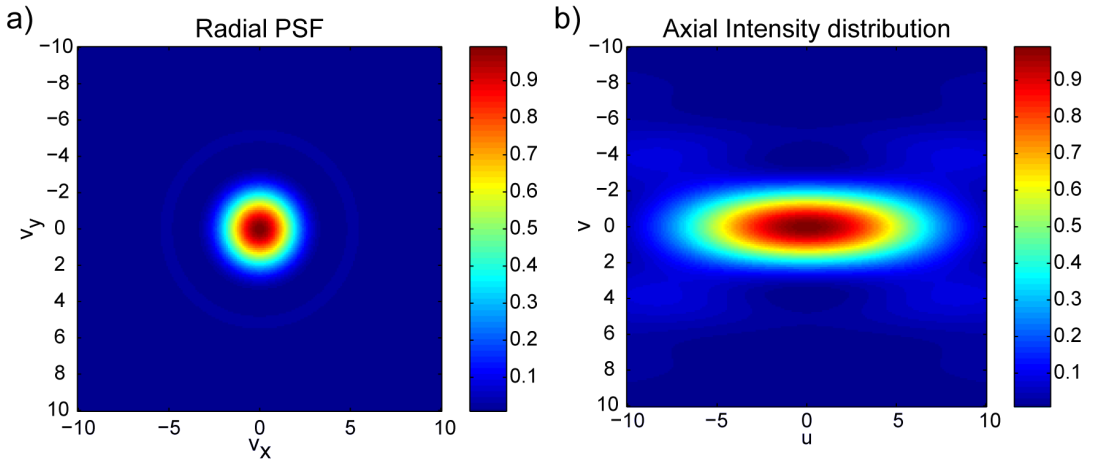

Figure 2.3.: a) Normalized intensity distribution in the focal plane and b) along the axial plane for an ideal circular lens with spherical surfaces in terms of the dimensionless units ν and u defined in the text.

geometric quantity.

To obtain a high value for the numerical aperture the angle of convergence α needs to go to $\pi/2$. Therefore a high NA-objective collects the light of an object over a large solid angle.

To express the point-spread-function in terms of dimensionless units in the following the radial optical coordinate ν as well as the Fresnel number N are introduced. The radial optical coordinate is defined as [14]:

$$\nu = \frac{2\pi}{\lambda}\frac{a}{f}r_3 \approx \frac{2\pi}{\lambda}r_3 \sin\alpha \tag{2.13}$$

Due to the factor $\sin\alpha$ the radial optical coordinate is proportional to the NA. Therefore for a fixed ν the real radial coordinate r_3 is anti-proportional to the numerical aperture in the focal region.

As third quantity the Fresnel number N is introduced.

$$N = \frac{a^2}{\lambda z} \tag{2.14}$$

It connects the area of the aperture with the wavelength λ and the image position z.

Inserting this quantities into Eq.2.11 and calculating the modulus squared delivers a compact expression for the radial intensity distribution at the focus.

$$I(\nu) = (\pi N)^2 \left[\frac{J_1(\nu)}{\nu}\right]^2 = I_0 \left[\frac{J_1(\nu)}{\nu}\right]^2 \tag{2.15}$$

This equation is often referred to as Airy pattern [14, 15]. In Fig.2.3.a) the normalized intensity distribution in the focal plane is shown. It is circular symmetric and consists out of a bright center peak followed by an infinite number of much darker concentric rings. According to

the Rayleigh criterion two points are barely distinguishable if the maximum of the first Airy pattern is in the first minimum of the second one [15]. Obviously points that are even closer can be distinguished if a sufficient signal to noise ratio has been reached, but it than requires a precise modeling of the PSF and fitting procedure. The intensity minima of Eq.2.15 only depends on the roots of the Bessel function $J_1(\nu)$. Since $\nu \propto r_3 \sin\alpha$ the resolution of an aberration-free imaging system depends only on the angle of divergence α and therefore on the numerical aperture. By setting $\nu = 3.8317$, which is the first minimum of the Bessel function, out of formula 2.15 an expression for the numerical aperture for a diffraction limited circular lens can be derived.

$$\text{NA} = 0.61\frac{\lambda}{r_{min}} \tag{2.16}$$

Where r_{min} is the radial distance of the first minimum in the object plane. Hence the numerical aperture of a diffraction limited imaging system is at the same time a measure for the resolution and light gathering ability.

To determine the intensity distribution in the axial plane for small displacements Δz from the focus in Eq.2.6 the focal plane is set to be z. The field in the new focal plane and hence the intensity distribution follows immediately. To express the intensity in dimensionless units the axial optical coordinate u is introduced:

$$u = \frac{2\pi}{\lambda}a^2\left(\frac{1}{f} - \frac{1}{y}\right) \approx \frac{2\pi}{\lambda}\Delta y\frac{a^2}{f^2} \tag{2.17}$$

In Fig.2.3.b) the radial intensity distribution in dependence of the axial position u is presented. Here ν is essentially a cut through the point-spread-function and u measures the defocussing. $u = 0$ when the system is focused. As one would intuitively expect from ray optics the signal is symmetric with respect to the focal plan for an imaging system free of aberrations.

2.3. Optical Transfer Function

Until now the imaged intensity distribution of a point-source was considered but in reality every object is extended. An spatial intensity distribution can be transfered into the spatial frequency domain, similar to an electrical signal in time-domain which is transfered into frequency domain. By means of Fourier transformation the amplitude of the different spatial frequencies $\xi = 1/L$ contributing to a signal are determined. The result is called the optical transfer function (OTF) of the system. In the one-dimensional case, as presented in Sec.2.2, the OTF can be represented as [17]:

$$\text{OTF} = H(\xi) = |H(\xi)|\exp\left(-i\Theta(\xi)\right) \tag{2.18}$$

Where $H(\xi)$ is the Fourier transform of the signal, $|H(\xi)|$ is the modulation transfer function (MTF) and $\Theta(\xi)$ the phase transfer function (PTF). To give a more intuitive picture the

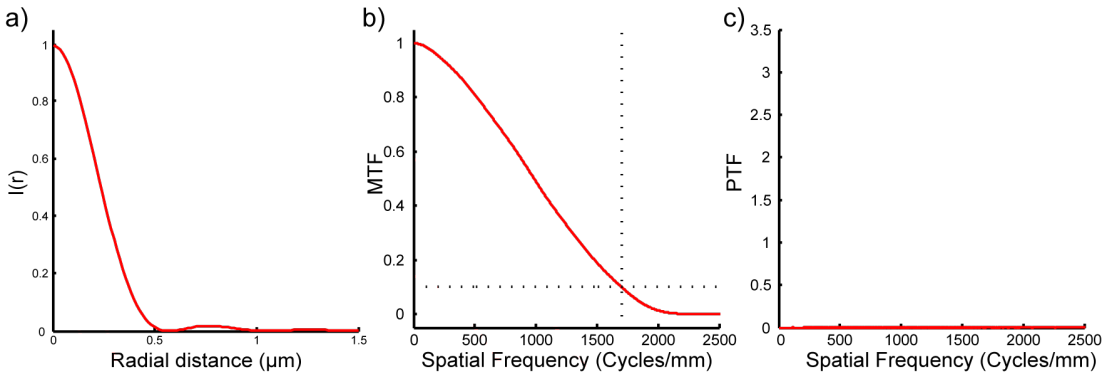

Figure 2.4.: a) Ideal point spread function of a focused imaging system. b) Modulation transfer function of the PSF shown in a). And c) the corresponding phase transfer function which does not suffer from phase jumps.

convolution theorem of the Fourier transformation can be used:

$$\mathcal{F}^{-1}\left(f * g\right) = \mathcal{F}^{-1}(f) \cdot \mathcal{F}^{-1}(g) \tag{2.19}$$

$$\mathcal{F}\left(\mathcal{F}^{-1}(f)\mathcal{F}^{-1}(g)\right) = f * g \tag{2.20}$$

According to Eq.2.6 the field in the focus of a lens can be interpreted as the two-dimensional Fourier transformation of the pupil function $P(x_2, y_2)$. In case of a homogeneous illuminated circular lens $P(x_2, y_2)$ is described by a circle and the Fourier transformed is $U = \mathcal{F}^{-1}(P(x_2, y_2))$. Hence the Fourier transform of the modulus squared of the field $\mathcal{F}^{-1}\left(U \cdot U^*\right)$ can be expressed by the convolution of two identical circles in spatial domain. The convolution yields:

$$U * U^* = \frac{-2\xi\sqrt{4-(2\xi)^2} + 4\arccos\xi}{2\pi} \tag{2.21}$$

This function is unity for $\xi = 0$ and drops monotonously to zero at $\xi = 1$. Obviously the convolution of two circles will drop to zero as soon as the distance between their centers is larger than two times the radius. Hence there will be a maximal frequency which is transfered by the imaging system. This cutoff-frequency is the reason why each lens acts as a low pass filter for spatial frequencies. In Fig.2.4 the point-spread-function, modulation transfer function and phase transfer function of a perfect imaging system is presented.

One possible definition of the term resolution is the inverse of the limiting spatial frequency where the MTF drops below a certain threshold. The MTF is a function which describes the ability to transfer each frequency through the imaging system while the resolution is a number describing only the limiting frequency. Therefore the MTF contains more information.

For an aberration free imaging system the point-spread-function is symmetric and the Fourier transformation real. Therefore the phase must be either 0 or π. This behaviour is presented in Fig.2.4c).

In case of an asymmetric PSF the phase transfer function can also take other values. Therefore the PTF is often used as optical design criterion to estimate the presence of aberrations.

2.4. Ray tracing

Finite ray tracing is an essential and universal tool in optical design of imaging systems [18]. Ray tracing is based on iterative application of translation and refraction by Snell's law to an optical ray passing through an optical system, similar to the ABCD formalism. While the ABCD formalism is only valid in the paraxial approximation, ray tracing can be applied for any propagation angle with respect to the optical axis since the refraction is calculated with exact trigonometric functions. Calculating a fan of rays by hand is computational demanding but using computers for the calculation made this method a powerful tool.

2.5. Optical Path Difference

The minimization of the optical path difference (OPD) to numerically calculate the focal point of an imaging system is a powerful tool. To apply the OPD the system has to be sufficiently optimized in the sense that geometric rays are imaged to a point smaller than the diffraction spot.

The optical path length d is the geometrical length l of an optical beam multiplied with the refractive index n of the medium. Hence the optical path difference (OPD) between two rays is defined as:

$$\text{OPD} = l_1 n_1 - l_2 n_2 \tag{2.22}$$

For an unperturbed system the wavefront impinging on the focus is perfectly spherical. Hence the OPD of two arbitrary chosen rays of the system is equal to zero. In a non-perfect imaging system the optical path length of the single rays fluctuates around a mean value.

To calculate the rms optical-path-difference a large number of rays and different points close to the optical axis are considered. Building the root-mean-square of the phase difference optimizes the system for a large field of view instead of a single point.

This method is used by the `OSLO` software to find the focus of a system automatically (see Sec.5.1).

2.6. Imaging with a high Numerical Aperture Objective

As shown in Sec.2.2 the resolution of a lens is directly connected to its numerical aperture. To achieve a high resolution the angle of convergence α has to be increased, but for large numerical apertures (NA ≥ 0.7) the paraxial approximation is no longer valid [14]. Therefore the following effects need to be consider:

- Apodization: The distribution of the light field at the position of the lens is in general a function of the divergence angle α.

- Depolarization: The wavefront of an incoming linear polarized beam focused by a high NA-objective is not uniform polarized in the focus. There all polarization field components have to be added up. Therefore treating light with a vectorial theory instead of a scalar theory is needed.

- Aberration: In general aberrations of an imaging system increase with its aperture size. Pronounced aberration cause significant deviations from a perfect Airy disk. Therefore the design of a high NA lens with a small amount of aberration is a challenging task.

2.6.1. Apodization

In Sec.2.1.2 the pupil function $P(r)$ for a circular lens was introduced. After passing through the lens the beam converges to the focus. Since for an ideal system the wavefront is spherical the distribution will become a function of the divergence angle α.

The function $P(\alpha)$ is the apodization function which is strongly related to the pupil function $P(r)$ which depends on the radius. The both are connected by the expression [14]:

$$P(\alpha) = P(r) \left| \frac{g(\alpha)g'(\alpha)}{sin(\alpha)} \right| \tag{2.23}$$

Where $g(\alpha)$ is the ray projection function and $g'(\alpha)$ its derivative with respect to α. Hence the pupil function is transfered into the angular dependent apodization function in dependence of the ray projection function. The exact form of the ray projection function strongly depends on the optical system.

2.6.2. Depolarization

To calculate the effect of depolarization a vectorial PSF analysis has to be fulfilled as done in e.g. [14]. A qualitative description can be achieved by the following geometrical considerations. Consider a collimated homogeneous beam with linear polarization in x-direction and a high NA-lens (see Fig.2.5.a)). Hence the electric field vectors in front of the lens is pointing into the x-direction. At the lens the electric field vectors get tilted by refraction, where the tilt angle strongly depends on the position on the beam. A tilt of the field vector is equivalent to the generation of field components into the corresponding direction.

The intensity in x-direction shows the well-known Airy pattern. There are no additional contributions since there is no field in y- and z-direction which can be tilted in this direction.

In the focal region the intensity z-component consists out of two spots separated by a dark strip through the y-axis, see Fig.2.5.a). The upper and lower field vector in the diverging region

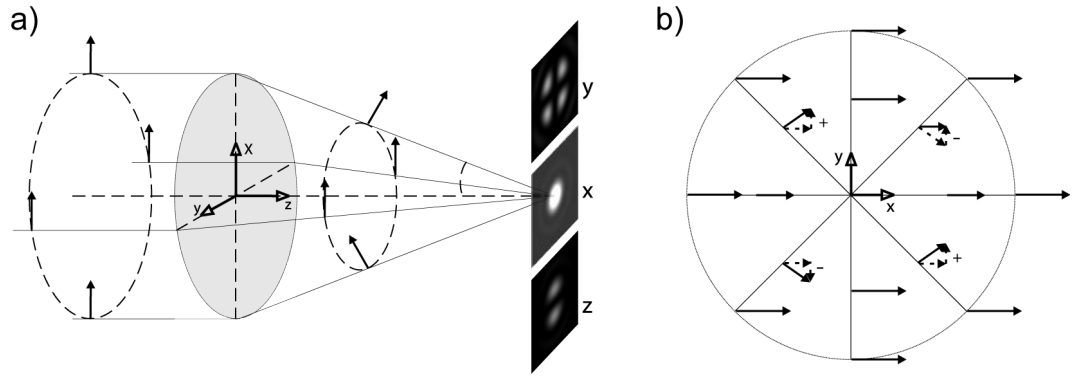

Figure 2.5.: a) Illustration of the depolarization effect. A collimated beam polarized in x-direction is focused by a high NA-lens (gray). The arrows indicate the direction of the field vectors. The small sketches show the intensity profiles at the focal plane in the corresponding direction. b) View along the optical axis illustrates the origin of the different sign in the phase for the field vector in y-direction at the xz-plane. [19]

obviously produce a intensity contribution in z-direction, while in the zy-plane no contribution is created.

In y-direction the intensity component consists out of four spots positioned in the four quadrants of the xy-plane. The dark strip along the y-axis is produced by the same effect as the one in the intensity z-component. Fig.2.5.b) illustrates the origin of the dark strip along the x-axis by destructive interference.

For a light-source emitting linear polarized light an polarization filter should be placed in front of the camera. In this way the intensity contributions in the other directions are eliminated.

2.6.3. Aberrations and Strehl intensity

In reality every imaging system suffers from aberrations. In wave optics this means that the wavefront converging to the focus is not spherical and in geometrical optics that not all rays are focused to the same spot. Aberration might be caused by imperfections in the lens design or by misalignment of single components of the system. In general aberration are more present for high numerical aperture systems.

There are various kind of aberrations which can be attributed to a deviation of the wavefront to a spherical reference sphere. Hence an aberration function Φ is introduced to describe the phase change of the secondary wave caused by aberration. Φ is often represented in terms of Zernike polynomials (see [15]). However giving a general expression for the aberrations of a distorted system is difficult. To determine the main aberration source of an imaging system the simplest way is to compare the measured intensity distribution with the characteristic ones of systems distorted by a certain kind of aberration.

In presence of aberrations the peak intensity is reduced since the imaged spot becomes bigger than that limited by diffraction. The Strehl intensity is a quantity that describes this effect

quantitatively and is defined as [14]:

$$i(\nu, \Psi, u) = \frac{I(\nu, \Psi, u)}{I_{wa}(\nu, \Psi, u)} \tag{2.24}$$

Where Ψ is the angle in polar coordinate representation, I is the intensity of the measured signal (with aberration) and I_{wa} the intensity of a system without aberration.

In general one is interested in the Strehl ratio S at $u = \nu = 0$ which is equivalent to the intensity ratio at the center of the intensity distribution. According to the Marechal criterion a system is called diffraction limited as long as $S \geq 0.8$, which corresponds to a rms wavefront deviation of $\lambda/14$ [20]. A reduced Strehl ratio corresponds to a lower contrast of the signal to the background.

2.7. Summary

To observe single atoms in an optical lattice diffraction limited objectives with a high numerical aperture are needed. The paraxial approximation is no longer valid for such devices due to the needed large divergence angle. Hence high quality aspherical lenses are needed to compensate for aberrations. In praxis high NA objective consist out of several lenses to reduce the optical refraction power at a single surface. In Ch.3 the properties of the objective to be analyzed are described in detail.

3. In-house developed microscope for single atoms

In this chapter the unique physical properties of the in-house designed diffraction limited microscope are introduced. Here the designed imaging characteristics as well as the physical dimensions are presented. Afterwards the assembly of the lenses ta a high precision lens-holder under clean room conditions is explained in detail.

3.1. Physical properties

The developed microscope is designed to observe single cesium atoms fluorescing on the D2-line ($\lambda_{\mathrm{D2}} = 852\,\mathrm{nm}$) trapped within a two-dimensional spin-dependent optical lattice. It works in the diffraction limited regime and consists out of an aplanatic solid-immersion lens and an aspheric lens (see Fig.3.1) both made out of N-SF10 glass with a refractive index of $n_{\text{N-SF10}}(852\,\mathrm{nm}) = 1.71$ [21]. A ray tracing analysis was used to calculate the aspheric deformation coefficients and the conic constants as well as the radius of curvature of the solid immersion lens [22].

The solid immersion lens increases the numerical aperture of the asphere by a factor of up to n^2 [23] by increasing the refractive index of a large portion of the medium between object and asphere. A similar technique is used in immersion oil microscopy, where numerical apertures of larger then unity can be achieved. By means of this technique the designed value of the numerical aperture is NA $= 0.92$, which is significantly larger than the state of the art in the field of cold atoms of NA $= 0.8$ in the group of M. Greiner [12]. A numerical aperture of this quality corresponds to a resolution of $R \approx 564\,\mathrm{nm}$ which is smaller than the lattice constant $a = 612\,\mathrm{nm}$ of the planned experimental apparatus. Therefore a diffraction limited imaging and addressing of the atoms with single lattice site resolution will be feasible.

The effective focal length (EFL) of the objective is EFL $= 12\,\mathrm{mm}$. In combination with the focal length of the imaging lens this quantity defines the overall magnification factor of the imaging system needed for the analysis of the measured data, see Ch.5. In the focal plane at a radial distance of the object to the optical axis of approximately $28\,\mu\mathrm{m}$ the Strehl ratio drops to $S \approx 0.8$. We take $S = 0.8$ as limiting criterion of the field of view. Hence the field of view has a side length of $56\,\mu\mathrm{m}$ which corresponds to 91 lattice sites.

The beam profile of the spin-dependent dipole trap is elliptical. To fill the whole field of view of the microscope the mayor axis ($200\,\mu\mathrm{m}$) of the ellipse is oriented perpendicular to the optical axis. A high intensity in the focal region is achieved by positioning the minor axis ($50\,\mu\mathrm{m}$) along the optical axis. The focal depth of the objective ($\Delta f < 0.8\,\mu\mathrm{m}$) is much smaller then

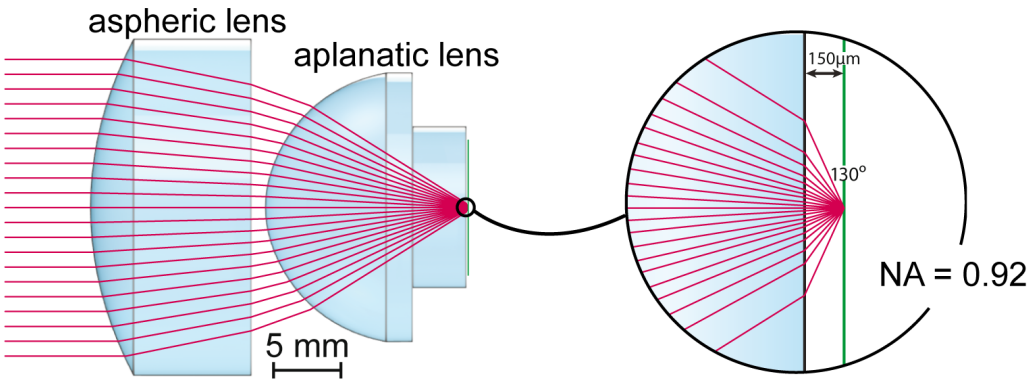

Figure 3.1.: Sketch of the diffraction limited objective for the observation of single atoms consisting out of an aplanatic solid immersion and an aspheric lens. The distance between both lenses is 1 mm and the focal point is 150 µm in front of the objective. The opening angle of $2\alpha = 130°$ corresponds to a numerical aperture of NA $= 0.92$.

the minor axis. To keep the atoms in focus an additional trap along the optical axis is needed. By means of retroreflection a dipole trap ($\lambda_{\text{Dipol}} = 1064\,\text{nm}$) in a standing wave configuration is realized. Hence a reflection coating for this wavelength is deposited on the planar surface of the solid-immersion lens. By this means atoms trapped in a knot of the standing-wave will have a constant distance to the objective and stay in focus, even if the objective is moving.

As a trade-off for the diffraction limited high numerical aperture the working distance of the objective is small. The closer the object to the first surface the more light is collected due to the immersion principle. To guaranty a sufficient amount of optical access to the focal point the working distance was chosen to be $d_{work} \approx 150\,\mu\text{m}$. This ensures that the high intensity dipole trap beams do not clip on the solid immersion lens and the optical molasses beams do not produce stray-light. The short working distance forces to place the objective directly into the vacuum chamber. Therefore all components of the objective including the glue have to be vacuum feasible.

In the later experiment there is no possibility to align the objective since it is directly placed into the vacuum chamber. To guaranty a correct positioning of the lenses towards each other a static aluminium oxide ceramic (Al_2O_3) holder with small mechanical tolerances ($1 - 3\,\mu\text{m}$) is designed.

For geometric reasons one of the magneto-optical-trap axis has to be transmitted through the objective. The cooling transition has the same wavelength as the observed fluorescence of the cesium atoms. Therefore the MOT-beam would cause stray light during the imaging. To overcome this problem a two-color MOT will be used, where the cooling beam along the optical axis uses the D1-line of cesium ($\lambda_{\text{D1}} = 895\,\text{nm}$).

3.2. Assembly under clean-room condition

The lenses of the objective and the ceramic lens holder were produced by two different companies and the assembly was self-made. In total two sets of lenses and two lens holder were delivered. Out of the surface data measured by the producing company (Aspheric on) the lens holder were designed for each of the lens sets separately. The marriage of lenses and holder was done in the Class100 clean-room[1] of the Center of advanced European studies and research (CAESAR). Clean room conditions guaranty that no major dust particles on one of the surface influence the imaging quality.

It turned out that for both lens sets the solid immersion lenses did not fit into the ceramic holder. This problem was solved by an iterative process of polishing and testing the match. Fine sandpaper (roughness $5\,\mu$m) was used to increase the inner diameter of the holder by polishing. Before testing the compatibility the holder was cleaned in an ultrasonic bath of first acetone and afterwards distilled water.

The lenses were placed in the holder and glued with a tiny droplet of aluminium filled epotek H77-glue, to fix the position towards each other. Holes are drilled into the lens holder to place the glue with a injection at the lenses, see Fig.3.2.a). For the evacuation of the volume between the lenses further holes access this space. A photography of the assembled objective is presented in Fig.3.2.b). Curing of the first objective was done over night at a temperature of $150\,^{\circ}$C. The heating from room temperature to the maximum temperature took $1.5\,$h as well as the cooling process. After the bake-out a crack at the edge of the aspherical lens near the adhesive point was observed. It was proven that the crack does not influence the imaging properties significantly since it is outside of the optical path, see Ch.6. To avoid damages on the second objective the curing was done at a maximum temperature of only $120\,^{\circ}$C and increased heat-up phase of $5\,$h. Additionally a balloon made out of aluminium foil around the objective prevents from local heating by air streams within the oven. This improvements resulted in an optical irreproachably objective.

After characterization of the optical imaging performance (see Ch.6) the undamaged objective was glued into the in-house built twelve sided vacuum chamber (see Fig.3.2.c)). Its design allows for maximal optical access and it is made out of SF57-glass which features low birefringence. A low degree of birefringence is needed in many experiments in quantum optics and due to the vacuum chamber we can avoid complicated alignment procedures, see [24]. Three droplets of the epotek H77-glue were used to fix the position of the objective within the chamber. The bake-out was done at a temperature of $120\,^{\circ}$C over night with a temperature gradient of $30\,^{\circ}$C/h during the heating and cooling phase. Close to one of the adhesive areas a small crack outside of the optical path in the glass cell was observed after cooling and transport back to the Institute. This is probably tension induced due to the different expansion coefficient of the materials ($\alpha_{\mathrm{SF57}} = 9.2 \cdot 10^{-6}$/K [21] and $\alpha_{\mathrm{Al_2O_3}} = 6 - 8 \cdot 10^{-6}$/K [25]). A length difference

[1] Less then 100 particles with diameter $\leq 0.5\,\mu$m per ft^3 (US FED STD 209E cleanroom standards)

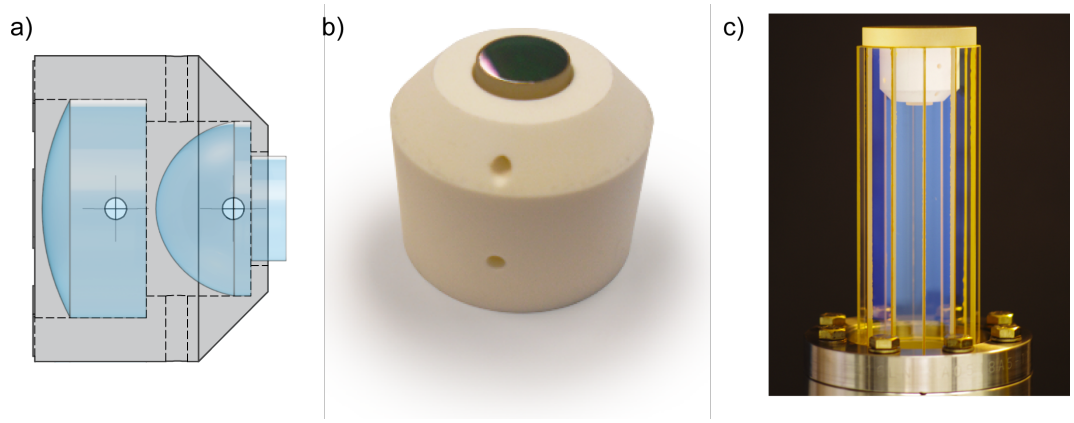

Figure 3.2.: a) Technical drawing of the holder including a set of lenses. b) Photography of the assembled Objective. The visible surface is the planar surface of the solid immersion lens with the reflection coating for $\lambda = 1064\,\text{nm}$. c) The objective of the microscope glued into the twelve sided vacuum cell.

between ceramic holder and glass cell of up to $\Delta L = 8.3\,\mu\text{m}$ between two adhesive points is calculated. Since the curing occurs at the maximum temperature this length difference leads to strains at room temperature. This constant strain makes the vacuum-cell objective system vulnerable for all kinds of shocks. Furthermore for future heating processes (e.g. vacuum bake-out) it has to be taken care to use small temperature gradients and a maximum temperature not higher than $T_{max} = 120\,^{\circ}\text{C}$.

4. Characterization Setup

In this chapter the set-ups used to characterize the objective of the microscope are described. In a first attempt a wavefront analysis was fulfilled. Afterwards the point-spread-function of a retroreflected beam and sub-micrometer scale light-sources was measured. The advantages and disadvantages of the different measurement methods will be discussed. Finally the obtained signals are compared with each other.

4.1. Wavefront analysis

For an unperturbed system a planar wavefront retroreflected by a combination of objective and mirror in the focal plane is expected to have a planar wavefront. Hence conclusions on the imaging quality can be drawn out of the wavefront after the retroreflection. In the following the set-up, which is sketched in Fig.4.1, will be described.

Light with a wavelength of $852\,\mathrm{nm}$ from a diode-laser in Littrow configuration is coupled into an optical single mode fiber in order to obtain a Gaussian intensity profile. The diameter of the collimated beam ($2\omega = 1.97\,\mathrm{mm}$) after transmission through optical fiber is magnified by a Galilean-telescope ($f_1 = -25\,\mathrm{mm}$, $f_2 = 500\,\mathrm{mm}$) by a factor of $M = 20\times$. Since the free aperture of the objective is in the order of $22\,\mathrm{mm}$ only the almost flat top profile in the center of the beam is used for the measurement. The outer part is clipped by the second lens of the telescope. We placed polarizers and waveplates in front of the telescope to control the polarization of the beam. Due to several mirrors and the beam-splitter wedge in the optical path the polarization of the beam at the position of the objective is not fully controllable. To check the collimation of the beam behind the telescope during the alignment a shear-plate-interferometer (Thorlabs SI254) is used. Afterwards the beam passes a beam-splitter wedge and is transmitted through the objective which is placed on a five-axis precision translation stage (Newport 9082V-M). In the focus of the objective a planar silver mirror performs the retroreflection. At this position a dielectric mirror has to be avoided because the reflection is distributed over several layers of the dielectric material and not on the surface. Therefore it is possible that the reflection depth is larger than the depth of focus of the objective. Furthermore the dielectric mirrors are designed to maintain the polarization under an incidence angle of $45\,^\circ$. A retroreflection under $90\,^\circ$ could change the polarization. These two effects would distort the measurement and lead to additional aberrations. The retroreflected beam passes the lens system a second time and is partially reflected onto the shear-plate-interferometer by the beam-splitter wedge. On the screen of the interferometer the interference pattern is observed to characterize the wavefront distortion due to the objective.

A large portion of the reflected light, which is transmitted through the wedge, is used to align

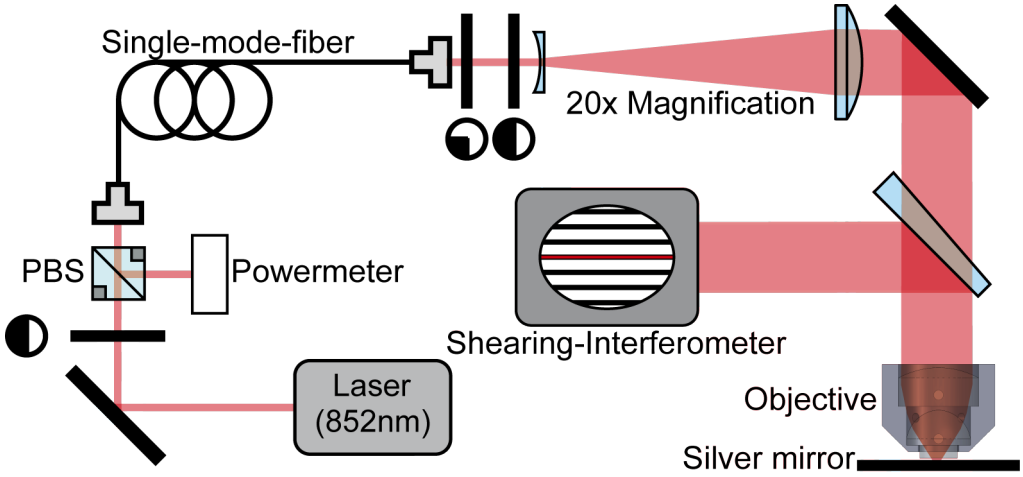

Figure 4.1.: Set-up to analyze the wavefront quality of a collimated beam after passing through the objective twice. The information on the wavefront is extracted by a shearing interferometer.

the system. It is ensured that the reflected beam overlaps with the incoming one by coupling this light back into the optical fiber and maximizing the transmitted light. At this point the high sensitivity of the system to vibrations due to the large beam-diameter becomes visible since the power measured after the fiber is fluctuating by $15\,\%$. Another problem is that this method does not align the angle of the objective to the optical axis. Already small misalignment angles will shift the reflection spot out of the field of view and therefore cause additional aberration.

Furthermore the planar silver mirror in the focus causes an inversion of the beam with respect to the optical axis. Due to the fact that the inverted beam passes the objective a second time the contribution of every aberration is mirrored to the opposite beam position. Hence the estimation of the wavefront quality will only deliver a lower bound.

The same set-up can be used to image the PSF by replacing the Shear-plate-interferometer by an imaging lens that focuses the collimated beam onto a CCD-camera. This measurement principle is similar to the one presented in Sec.4.2.2 and Sec.4.2.3. Here it has to be pointed out that in this set-up no point-like light-source is imaged. The size of beam on the mirror surface is assumed to be in the order of the diffraction limited spot.

4.1.1. Shear-plate-interferometer analysis

To extract information on the wavefront distortion due to the objective a shearing-interferometer was used. The shearing interferometer is based on interference of a beam with a copy of itself. The reflections on a planar glass plate on the first and second surface are used as the two interferometer signals (see Fig.4.2.a). For a collimated beam interference strips parallel to the reference line are observed.

The system was aligned by optimizing the parallelism to the reference line. In Fig.4.2.b the interference pattern of the retro-reflected beam is depicted. The interference signal is not of perfectly line shaped but shows some unevennesses which are indications for wavefront distor-

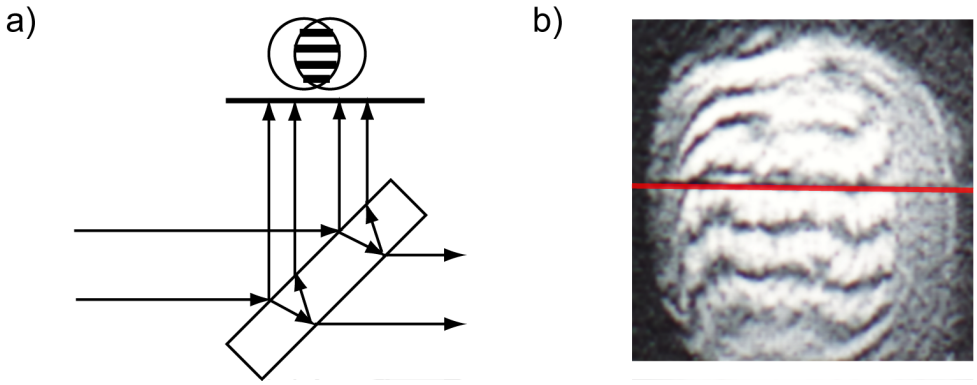

Figure 4.2.: a) Basic principle of a shearing-interferometer. An incoming beam is reflected on both surfaces of a planar glass-plate. The interference pattern of both beams is observed on a screen. b) The measured interference pattern of a collimated beam after passing through the objective twice. The reference line is marked in red.

tions. Nevertheless the universal behavior of the lines shows a tendency to be parallel to the reference line. At the edge of the signal the interference pattern bends away from the reference line so the wavefront quality seems to change over the aperture. The radius of curvature of the wavefront is calculated according to equation:

$$R = \frac{s \cdot d_f}{\lambda \sin \gamma} \tag{4.1}$$

Where s is the shearing distance, d_f the fringe distance and γ the angular deviation of the fringes to the reference line. Out of Fig.4.2 a radius of curvature of $R = 114.9\,\mathrm{m}$ over $80\,\%$ of the aperture is calculated. Due to the quality of the signal this results can only be considered as a first hint of a properly working imaging system.

4.1.2. Shack-Hartmann wavefront sensor

A Shack-Hartmann wavefront sensor (Thorlabs WFS150-5C) was used to measure the root-mean-square wavefront deviation quantitatively. Due to small the detector size of $5.95 \times 4.76\,\mathrm{mm}^2$ the beam could not be analyzed as a whole. In the center region a rms wavefront deviation of less than $\lambda/10$ was measured. The attempt to write a stitching routine that combines several sensor signals failed due to the low number of pixels of the sensor and the sensitivity of the system to environmental influences which change the measured wavefront on short timescales of several seconds.

4.2. Measuring of the Point-Spread-Function

The basic idea is to use a light source with a diameter much smaller than the smallest resolvable distance and image it with the objective and a second lens onto a CCD-camera to measure the point-spread-function. Out of the PSF the characteristic values of the objective, especially the numerical aperture and Strehl ratio, can be extracted. Due to the high resolution of the microscope the challenge is to find a light-source whose aperture is much smaller than $500\,\text{nm}$. At the same time the light source has to emit enough light to observe it with the CCD-camera. Three different kind of light sources were tested and the retroreflected configuration (see Sec.4.1) was modified to image the PSF. The first approach was to image a pinhole ($\varnothing = 100 - 300\,\text{nm}$) illuminated from the backside. Afterwards nanoparticles of well defined size ($\varnothing_{\text{PMMA}} = 400\,\text{nm}$ and $\varnothing_{\text{TiO}_2} < 25\,\text{nm}$) were excited to fluoresce. Finally the aluminium coated tip of a Scanning-Near-field-Optical-Microscopy (SNOM) fiber with a free aperture of $a < 200\,\text{nm}$ was used. All measurements were performed with light of wavelength $\lambda = 852\,\text{nm}$ which is equivalent to the design wavelength of the objective.

4.2.1. Pinhole approach

Illuminating a pinhole of diameter $\varnothing \ll 564\,\text{nm}$ will create a high NA light-source. It was planned to drill the pinhole by a fast ion beam (FIB) into a metallic substrate, since no commercial pinhole with apertures of the needed size are available. In the first test a gold-layer of $220\,\text{nm}$ thickness is sputtered onto a microscopy glass surface. According to Lambert-Beers law we expect an attenuation of $1 : 7.8 \cdot 10^7$ but an attenuation of only $1 : 3000$ is measured. Holes with diameters between $100\,\text{nm}$ and $320\,\text{nm}$ were produced with a FIB at the CAESAR-institute. An imaging of the pinholes is not possible since the transmission through the pinhole was in the same order of magnitude as the direct transmission through the gold layer. The low attenuation factor is probably due to the rough gold surface with a lot of inhomogeneities (see A.2) typical for sputtered gold films [26].

In the second attempt a $10\,\text{nm}$ layer of chrome is placed on a microscopy plate to increase the adhesion of the gold layer on the glass. Afterwards a gold-layer of approximately $500\,\text{nm}$ thickness is evaporated. Heating of the glass plate with the gold layer to $500\,^\circ\text{C}$ is done to anneal the roughness of the gold layer. The attenuation is measured to be $1 : 370\,000$. After the production of the pinholes in the FIB-device macroscopic holes are observed in the substrate, which are visible by the bare eye. Residuals which expanded in the vacuum of the FIB probably caused this damages.

The approach of imaging a pinhole was rejected since in the meantime different methods turned out to work well.

4.2.2. Imaging of Nano-particles

In the second attempt of imaging a light source with an aperture much smaller than the resolution of the objective nano-particles were used. The excitation of the particles is done by an evanescent light field to avoid any stray-light.

Adopting the principle of total internal reflection fluorescence (TIRF) microscopy [27] the nano-particles are placed on the surface of a prism and illuminated by an evanescent light field, see Fig.4.3. The evanescent field is created by illuminating the prism under an angle of total internal reflection from the backside, see Fig.4.3.b). Hence an exponential decreasing field penetrates into the air and couples to the nano-spheres on the surface. A Codexx-polarizer in combination with a $\lambda/2$-plate is used to tune the incoming linear polarization to p-polarization for high transmittance because the amplitude of the transmitted light field strongly depends on the incoming polarization [28, 29]. To increase the amplitude of the evanescent field the beam is focused to a spot of radius $r \approx 10\,\mu\text{m}$. The light emitted by the particles is collected by the objective which is placed one working distance away from the prism. For the positioning of the objective in front of the prism again a five-axis translation stage with a translation of $4.4\,\mu\text{m}$ per $5\,^\circ$ turn was used. A plano-convex lens images the signal onto a CCD-camera which is placed in its focus. The diameter of the lens is 2 inches to avoid clipping and the focal length is $f = 750\,\text{mm}$. Hence the magnification M of the imaging system is $M \approx 63.79\times$ and we expected the first minimum of the PSF at $x_{min} \approx 36\,\mu\text{m}$ in radial direction in the image plane which corresponds to approximately 8 pixel. The size in the object plane is calculated by considering the magnification factor of the system. To filter the light from the intensity components produced by depolarization (Sec.2.6.2) a linear polarizer is placed infront of the camera.

We used nano-particles made out of polymethly methacrylate (PMMA) with a diameter of $\varnothing_{\text{PMMA}} = 400\,\text{nm}$ and titanium dioxide (TiO_2) $\varnothing_{TiO_2} < 25\,\text{nm}$. For the deposition of the nano-particles on the surface of the prism the particles were solved in high quality distilled water with a conductivity of less then $0.005\,\mu\text{Sv/cm}$. A droplet of the solvent was placed on the acetone cleaned prism surface and subsequently the water evaporated. The residuals on the surface now mainly consist out of particles of known size.

In this set-up it is impossible to determine the exact number of observed particles contributing to a PSF signal. An accumulation of particles leads to an increased light-source size and therefore to a distorted PSF. Signals of comparatively low brightness are chosen since the probability to image more then one particle is decreased.

Between the objective and the plano-convex lens a manual iris diaphragm can be build in to enable the tuning of the numerical aperture and Strehl ratio by reducing the free aperture. It also allows for easier alignment of the optimal working point in the later experiment. A first characterization of the numerical aperture versus the aperture diameter was performed (see Sec.6.4).

An advantage compared to the wavefront analysis configuration is that the light passes the

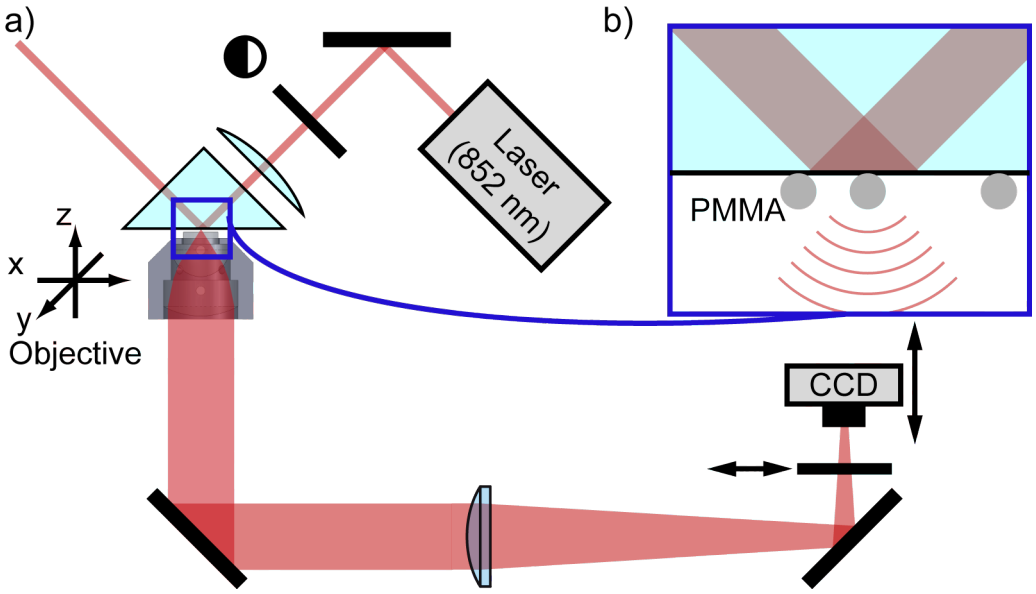

Figure 4.3.: a) Set-up for imaging of nano-particles with the microscope onto a CCD-camera. b) Origin of the high NA light source by coupling an evanescent field to nano-particles. The evanescent field is created by total internal reflection.

objective only once. Therefore possible aberrations are not artificially enlarged. However this setup also includes some major disadvantages. The exact position of the illuminating beam on the surface of the prism with the nano-particles can only be estimated due to refraction at the surfaces. This complicates the alignment procedure. Further disadvantages are the limited amount of light as well as the uncontrollable polarization of the light emitted by the particles. In combination with the depolarization effects of the objective (see Sec.2.6.2) this may cause asymmetries in the measured signal.

4.2.3. Imaging of a SNOM-fiber tip

In another approach the aluminium coated tapered tip of a SNOM-fiber (Lovalite E50-MONO780-AL-200) was used as a point-like light source to measure the point-spread-function. The aperture of the SNOM tip has a diameter of approximately 200 nm. A three axis translation stage (Thorlabs MAX302/M) was used to change the position of the fiber in front of the objective. This enabled us to place the fiber in the focus of the objective with sub-micrometer precision. Moving the light-source instead of the objective turned out to simplify the alignment procedure significantly. The five axis of the objective were used to align the objective parallel to the optical table.

To control the polarization of the light at the tip a combination of polarizers and wave-plates is used in front of the fiber coupler. The aim is to achieve almost pure linear polarized light which is imaged by the objective and the plano-convex lens onto a CCD-camera. Again a Codexx-polarizer directly in front of the camera eliminates the polarization which

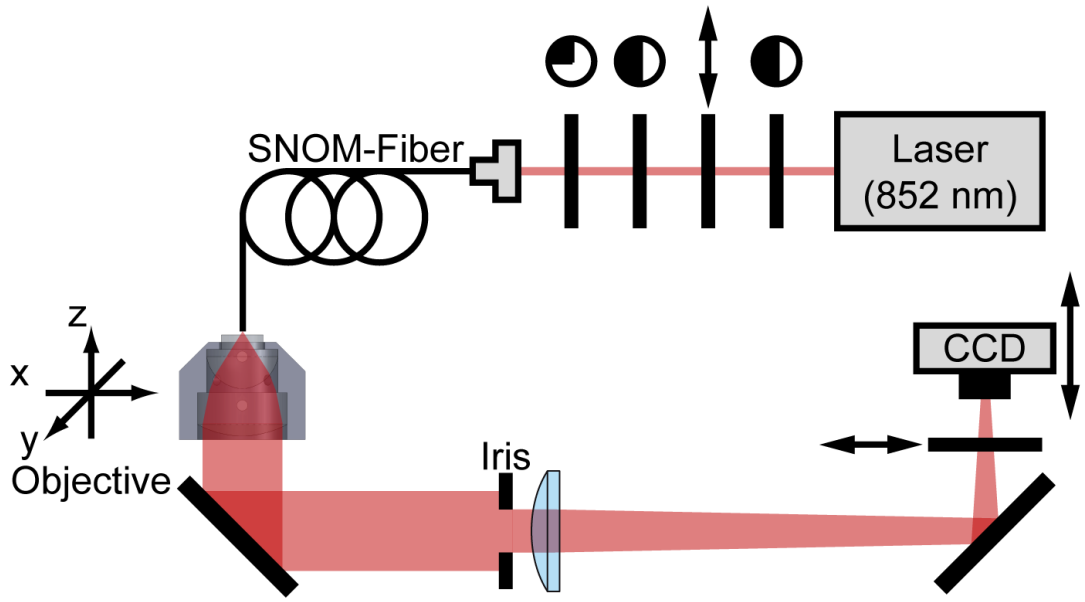

Figure 4.4.: Sketch of the characterization set-up. The light emitted by a SNOM-fiber tip is collected by the objective and imaged onto a CCD-camera by a plano-convex lens.

is created by depolarization effects in the objective (Sec.2.6.2). Additionally the polarization controlling elements in front of the fiber act as variable attenuator to assure that the power is below the damage threshold ($T_{damage} = 400\,\mu W$) of the Al coated fiber tip. This comparatively high power allows to use a new set of plano-convex lenses with focal length between $f = 1000 - 1500\,mm$ to increase the magnification factor to $M = 83\times - 125\times$ respectively. The power is not sufficient for a wavefront analysis by the shearing interferometer due to the large collimated beam diameter behind the objective. Furthermore the alignment is more complicated since the beam can only be observed by the beam-profile camera.

Any contact will inevitable destroy the tip because of the fact that the it is a very small structure. Therefore handling the fiber has to be done with greatest caution. The last centimeter has no robust protective but a sensitive aluminium coating. Fixing of the fiber was done a few millimeter away from the edge of protective coating to avoide damages in the aluminium layer. Hence the system is sensitive to vibrations and air flows which will especially for long exposure times lead to a blurring of the signal. To reduce this effect a shielding made out of aluminium foil was used against air flows. Additionally the flow-box of the optical table had to be turned off to avoid a continuous jittering of the signal.

4.3. Comparison of the measurement methods

In Fig.4.5.a-d the typical measured intensity distributions for the three different characterization configurations are shown. The peak intensity of all graphs is normalized to the corresponding

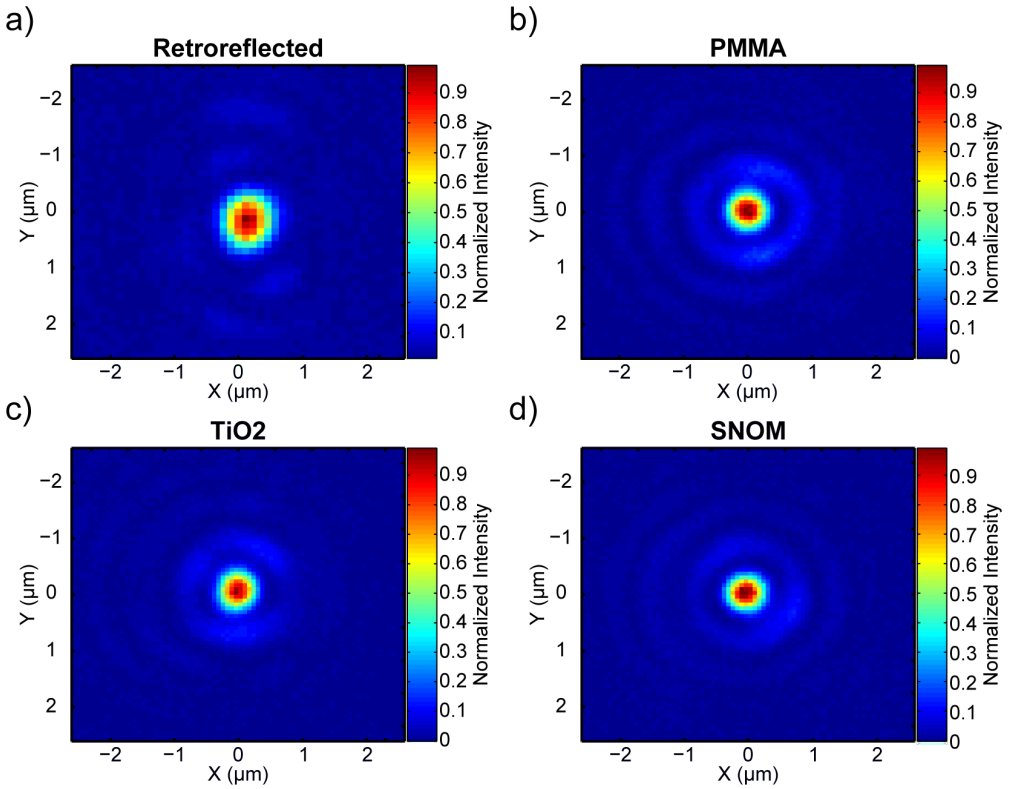

Figure 4.5.: Typical normalized intensity distribution measured for the different characterization setups. The graphics show a region around the peak of the distribution of approximately $5 \times 5\,\mu m^2$ with respect to the object plane. All signals are normalized to the maximum of the respective distribution.

maximum intensity value. Here as well as in all other presented data the scales refer to the object plane.

For the retroreflected set-up strong depolarization effects are observed in the region of the first side peak. Also the zeroth order peak shows a non-circular structure. The lower resolution is due to the different focusing lens ($f = 500\,\text{mm}$) in this setup. Therefore a smaller magnification of $M \approx 42\times$ was achieved. The in Sec.2.6.2 deduced cross-structure due to depolarization is nicely visible and prohibits an accurate analysis of the PSF. While a estimation of the numerical aperture out of the position of the first intensity minimum might be possible, a proper calculation of the Strehl ratio is unfeasible.

PMMA nano-spheres show a much better circularity but there is still some inhomogeneity left. Therefore one expects different results for the numerical aperture and Strehl ratio in dependence of the chosen axis. The diameter of $\varnothing = 400\,\text{nm}$ compared with the resolution of $R \sim 560\,\text{nm}$ permits calling the particles a point-source. Nevertheless the signal has a remarkable quality. The TiO_2 particles show a similar behavior with a less pronounced asymmetry, probably due to the smaller size. A rotation of the objective did not change the orientation of the signal and therefore dedicates the asymmetry to the light-source. This intensity signa-

ture might be explained by radiation characteristics of the nano-spheres which was shown to be in a shape similar to the observed one [30]. An asymmetric illumination can lead to an inhomogeneous pupil function and hence the observed signals.

Imaging of the SNOM-fiber tip leads to the signal with the smallest degree of asymmetry, see Fig.4.5.d). Also for tapered tips the radiation characteristics are not expected to be spherical symmetric [31], so the remaining asymmetries might be explained in a similar way as for the nano-particle configuration. The SNOM-fiber configuration was used for the final objective characterization because of the quality of the signal, the relatively large amount of light and the relatively easy alignment procedure.

5. Analysis Software

While the last chapter focused on different methods on how to create and image an ideal point source with our objective, this chapter focuses on the subsequent data-analysis. This analysis extracts the NA and Strehl ratio from the measured data. To achieve this two parts of software are required: A commercially available ray tracing software OSLO and various self written scripts in MATLAB. OSLO allows us to compare the measured signal with simulated signals for various aberrations to get an estimate of possible misalignments. Furthermore MATLAB was used to automatize this process. Additionally MATLAB was used to write scripts that determine the numerical aperture and Strehl ratio from the measured signal.

5.1. OSLO-Software

To generate a simulated PSF the objective and the used imaging lens are modeled in OSLO. For simplicity the mirrors of the setup are neglected since we can assume that the main source of aberration is the objective. The point source, also called object, is placed on axis, one working distance ($d_{work} \approx 150.3\,\mu m$) away from the first surface of the objective lens. The distance between both lenses of the objective ($d_1 \approx 1\,mm$) as well as its surface properties are taken from the original design. To check if this part of the system is modeled correctly the collimation of the beam behind the objective is analyzed in terms of the root-mean-square OPD.

The distance between the objective and the imaging lens (in future "lens$_2$") was set to be $d_2 = 350\,mm$ and is equivalent to the measured distance on the optical table. The radius of curvature, the thickness and the refractive index of lens$_2$ are taken from the data-sheet [32]. Finally the distance from the imaging lens to the image plane (d_3) is adjusted by minimizing the root-mean-square optical-path-difference. The modeled optical system is sketched in Fig.5.1.

Self-written OSLO-scripts are used to calculate the one dimensional PSF and MTF in dependence of the parameter to be analyzed. The intensity of the PSF is normalized to the maximal intensity of a perfect Airy disk such that the peak of the intensity distribution is equivalent to

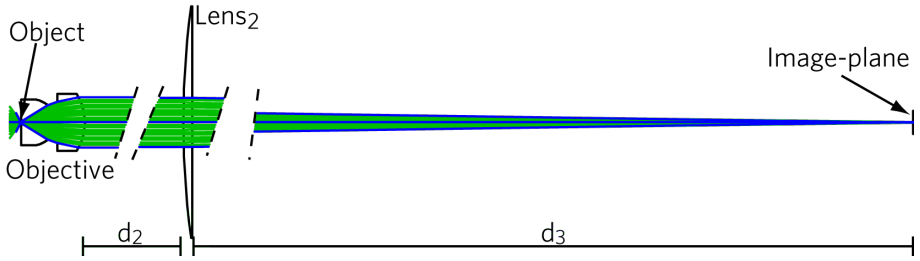

Figure 5.1.: Imaging system as it is depicted by the OSLO-software. Furthermore some of the adjustable dimensions are marked.

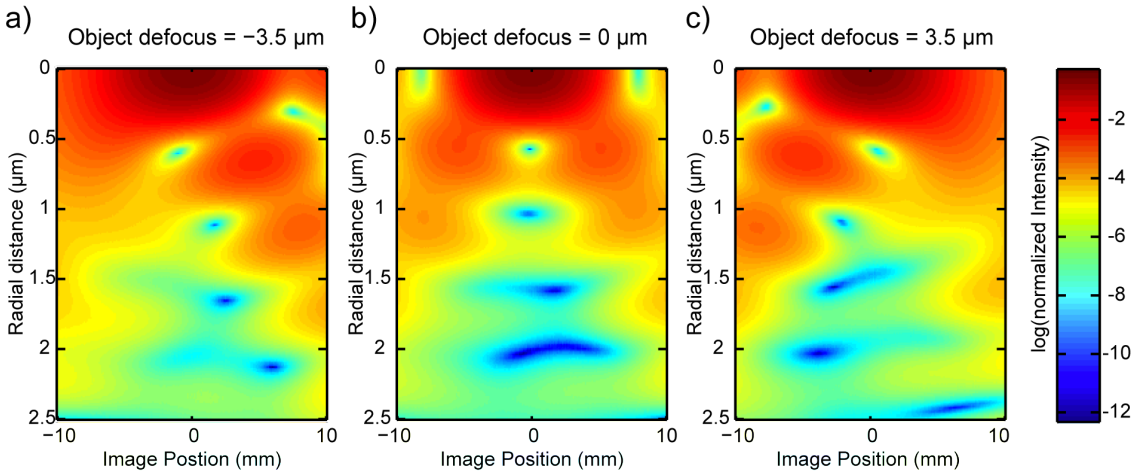

Figure 5.2.: Calculation of the logarithmic normalized intensity distribution in the axial plane for three different object positions around the focus of lens_2. Nicely visible are the spherical aberrations induced by the defocus, which lead to strong asymmetries in the axial plane.

the Strehl ratio. The simulated data is saved to `ASCII`-file-files, which are used in MATLAB.

5.1.1. Scan through focus

Based on the model described in Sec.5.1 the radial PSF in the dependence of an axial defocused light source was analyzed. We define a negative defocus as a reduction of the distance between lens and object. The results are used later to compare the measured to the simulated signal to achieve an estimation of possible misalignments, see Sec.5.2.5.

An `OSLO`-script scans the object in a distance of $d_{\text{scan}} = \pm 10\,\mu\text{m}$ around the focus of the objective. The step-size was set to $\Delta d_{\text{scan}} = 0.5\,\mu\text{m}$. This misalignment was partially compensated by refocusing the distance from the imaging lens to the camera d_3. The criterion of a well aligned system for the automatic focusing function is the minimal root-mean-square optical-path-difference. It is possible that various components (objective, imaging lens) of the experimental setup, described in the previous chapter, are misaligned. Therefore the influence of the defocused object is analyzed in the imaging plane by scanning through the optimal position ($d_{\text{scan,image}} \pm 10\text{mm}$) with step size $\Delta d_{\text{scan,image}} = 0.1\,\text{mm}$. The defocus of the object and the difference in d_3 are both saved. In the analysis method described in Sec.5.2.5 this information will be used to estimate the distance of the image plane to the perfect working point. For each position the one dimensional PSF was saved into a `ASCII`-file.

Subsequently the data is further analyzed in `MATLAB`. A two dimensional array is generated for each position of the object, which contains the one dimensional PSF for each image plane position. In other words the data of the axial intensity distribution around the focus was calculated similar to that shown in Fig.2.3. To give an impression on the influence of the defocus in Fig.5.2 for a small number of object positions the axial intensity distribution is presented. For better visibility of low intensity features the normalized intensity is presented with logarithmic

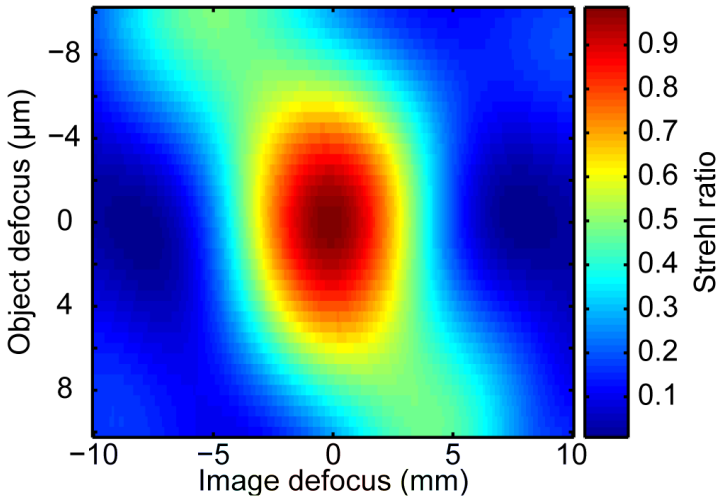

Figure 5.3.: Strehl ratio vs. defocusing of the object and image plane. Due to the small focal depth it is expected that the Strehl ratio drops below the diffraction limit for displacements of $\Delta L_{\text{object}} = 3.5\,\mu\text{m}$.

scale. Spherical aberration due to the defocus of object cause a strong asymmetry in the intensity distribution in the graphs a) and c). As expected from theory the partially compensation of the spherical aberration by lens$_2$ caused a shift of the optimal focal position of lens$_2$. For instance a defocus of $5\,\mu\text{m}$ causes a shift of the focus of lens$_2$ by approximately $25\,\text{mm}$.

Due to the spherical aberration the intensity in the side peaks of the Airy pattern at the focal position is increased and the Strehl ratio decreases dramatically. For a defocus of the object by $3.5\,\mu\text{m}$ the Strehl ratio drops below the diffraction limit of 0.8. This can be seen in Fig.5.3 where the Strehl intensity is plotted versus the defocusing of the object and image plane. For a large defocus of the object (defocus $> 5\,\mu\text{m}$) the maximum value of the Strehl intensity is not at the calculated focus of lens$_2$. Here the automatic focusing criterion of the OSLO-software fails in finding the optimal working point. Strong deviations of the wavefront to the reference sphere due to increasing amount of spherical aberration cause this effect. In the analysis software (Sec.5.2.5) the image defocus Δz with the highest Strehl ratio has to be considered while calculating the optimal image plane position. This is accomplished by adding Δz to the calculated focal distance d_3 of the imaging lens.

5.2. MATLAB-Software

The signal of the beam-profile camera was saved as a two dimensional array where each entry contains the integrated intensity measured over the corresponding pixel (pixel-size $4.4 \times 4.4\,\mu m^2$). Several MATLAB-routines were implemented to extract the relevant quantities and compare the measurements with the modeled intensity distributions. With the help of these analysis scripts the numerical aperture, Strehl ratio and also the axial displacement of the light-source from the optimal working point were calculated. Knowing this displacement is an important knowledge during the alignment process of the optical system.

5.2.1. Data processing

This section describes the transformation of the two-dimensional intensity distribution measured by the camera into a radial intensity distribution. Representing the data in one dimension will enable us to extract the numerical aperture and Strehl ratio in the later, see Sec.5.2.2.

In a first step the program locates the position of the maximal intensity which is assumed to be the center of the PSF. By this means the center is determined to an area of one pixel corresponding to $68 \times 68\,nm^2$ in the object plane. A higher spatial precision of the peak position is obtained by fitting a two-dimensional parabola to a region around the maximum with a side length of 9 pixel. This improves the accuracy of the center position by a distance of up to 0.5 pixel $\equiv 34$ nm in both dimensions.

For the reduction of local disturbances the analysis is based on the assumption that the measured signal is perfectly circular symmetric. As was shown in Fig.4.5.d) this assumption is justified and allows a transformation of the two dimensional into a one dimensional radial intensity distribution. As a further assumption the intensity measured at each pixel is assumed to impinge in center of it. In this way the distance between the center of the intensity distribution and the center of each pixel is set as the radial position with its appropriate intensity. Figure 5.4.b) shows the radial intensity distribution vs. the radial distance, measured by the camera and analyzed as described above. The distribution shows the familiar shape of the 1D Airy pattern.

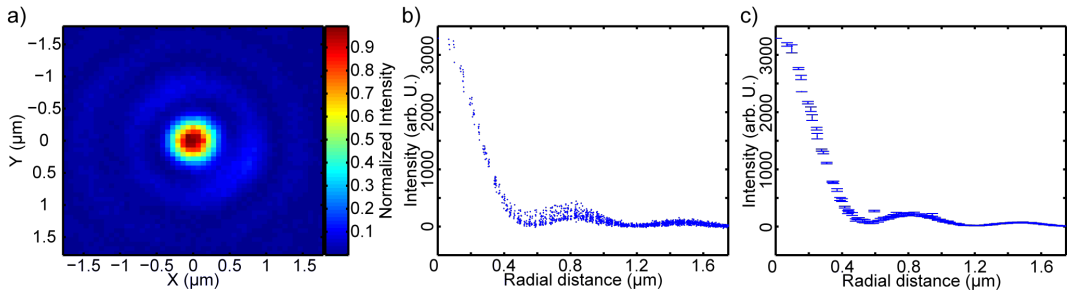

Figure 5.4.: Measured intensity distribution of a SNOM-fiber tip a), after transforming into a one dimensional radial distribution b) and after the binning process c).

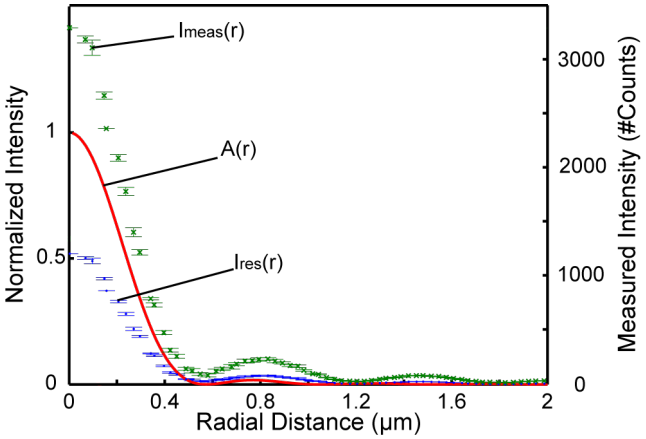

Figure 5.5.: In green the unscaled measured data in counts of an arbitrary unit (right Y-axis) is presented. The same data (blue) after rescaling to a perfect Airy pattern (red) normalized to unity, left Y-axis.

Furthermore the data is transfered into bins with 1 µm width (Fig.5.4.c)). For similar radial positions several intensity values are present because of the conversion into the one dimensional intensity distribution. Due to the small remaining asymmetry of the signal and background noise on the CCD-chip a spread of the distribution is observed. During the binning process the intensity as well as the radial position of each bin were set to the mean values of the data-points within the bin. The error on the intensity was set to the standard error on the mean [33].

5.2.2. Calculation of the numerical aperture and Strehl ratio

In the following the `MATLAB`-scripts used to extract the numerical aperture and Strehl ratio out of the binned radial intensity distribution (see Sec.5.2.1) are described.

The numerical aperture of the imaging system is extracted out of the position of the first minimum in the intensity distribution according to Eq.2.16. A polynomial of third order is fitted to the region around the minimum by the least square method weighted over the intensity error. The position of the minimum is extracted out of the fit-parameters by calculating the roots of the first derivative of the polynomial. According to Eq.2.16 the numerical aperture is calculated under consideration of the magnification factor. Gaussian error propagation leads to the value of the error ΔNA.

The intensity $I_{\text{meas}}(r)$ is measured in counts of an arbitrary unit, see Fig.5.5. To compare the measured values with the normalized intensity of a perfect Airy pattern a rescaling of the intensity values is needed.

$$I_{\text{res}}(r) = I_{\text{meas}}(r) \cdot C_{\text{res}} \tag{5.1}$$

Where $I_{\text{res}}(r)$ is the rescaled intensity and C_{res} the rescaling factor. The rescaling factor can be expressed as:

$$C_{\text{res}} = \frac{\int\int A(x,y)dxdy}{\int\int I_{\text{meas}}(x,y)dxdy} \tag{5.2}$$

Here the numerator is the two dimensional integration over a perfect normalized Airy pattern with the measured numerical aperture $\mathrm{NA}_{\mathrm{meas}}$. The denominator is equivalent to a summation over the intensity of all pixels multiplied with the detector area within the region of interest. We defined the region of interest as the detector area where the image is larger than the noise of the camera. For the measured signal this corresponds to radial distances of approx. $3.4\,\mu\mathrm{m}$, including 5 rings in the theoretical Airy disc. The denominator therefore can be understood as the measured power of the signal. Due to energy conservation aberrations can shift the intensity distribution but not reduce the overall power. Therefore the rescaling has to be interpreted as a equalization of the power of measured and ideal intensity distribution.

The estimated error on C_{res} depends on the error of the measured power and the one of the integral over the perfect Airy pattern. The later one only depends on the NA and is therefore directly connected to Δr_{min}. Hence the error is calculated as the difference between the integral with its minimum at r_{min} and $r_{min} + \Delta r_{min}$. The estimation of ΔP_{meas} is based on the observation of the intensity fluctuations of a single pixel. Observed fluctuation are in the order of $\Delta I \approx 4\,\%$ and the error on the total power is $\Delta P_{\mathrm{meas}} = 0.05 \cdot P_{\mathrm{meas}}$. ΔC_{res} is calculated according to Gaussian error propagation.

After rescaling the Strehl ratio can directly be read of as the intensity value at $I_{\mathrm{res}}(r = 0)$. A polynomial fit to the peak is performed to reduce uncertainties of the single measurement point. The error on the Strehl ratio ΔS follows from the uncertainties of the polynomial fit to the peak.

5.2.3. Calculation of the Modulation Transfer Function

To receive information on the amplitude of the spatial frequencies of the signal a fast Fourier transformation (FFT) is applied to the spatial intensity distribution. Hence the optical transfer function is obtained from the binned intensity data (see Sec.5.2.1). The frequency spectrum is interpolated by the use of the zero-padding method. Here a large number of zeros is added to the spatial signal to increase the sampling rate. The modulation transfer function is obtained by taking the absolute value of the OTF. Afterwards the spatial coordinates are used to generate the corresponding k-vector. This is done by the following equation:

$$\xi_k = \frac{k}{n \cdot \Delta x} \tag{5.3}$$

Where Δx is the distance between neighboring radial position values, n is the number of entries in the FFT and k is the index. Finally the absolute value of the padded FFT is plotted vs. the k-values.

Multiplying kth entry of the FFT-vector with the term $\exp(2\pi i \xi_k)$, where ξ_k is the spatial frequency, to the calculated FFT redefines the phase to be real.The phase transfer function is obtained by using `MATLAB` phase angle function. Plotting the PTF-values vs. the spatial frequency ξ illustrates the desired quantity.

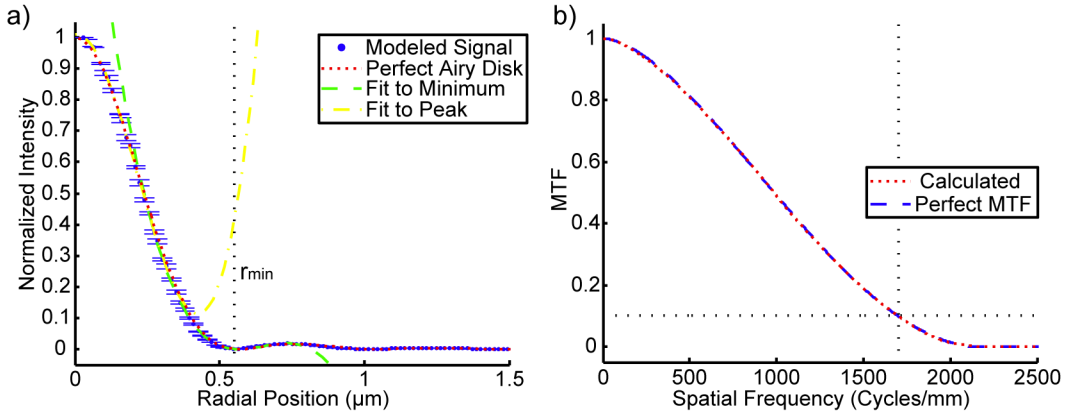

Figure 5.6.: a) Radial normalized intensity distribution of the modeled detector signal in the object plane. Furthermore the fit to the minimum (green) and the peak of the distribution (red) are presented. In red the perfect Airy pattern for the calculated NA is shown b) The MTF of the modeled detector signal (red) as well as the one of the calculated one (blue).

5.2.4. Application on modeled detector Signal

To evaluate the quality of the analysis method described in Sec.5.2.2 the detector signal of a perfect Airy disk is modeled and analyzed. According to equation 2.15 a two dimensional array containing a perfect Airy disk with an numerical aperture NA $= 0.92$ is created. The scale of the array is chosen in a way that ten entries correspond to one pixel-length in the object plane ($l \approx 69\,\text{nm}$). A random shift of the center of the Airy pattern ensures that the analysis does not rely on the peak position. Summing up the intensity values of a rectangular with 10×10 entries yield the integrated intensity of a artificial pixel. Doing so over the whole array yields a camera signal of 240×320 pixel.

This procedure was repeated for 25 randomly distributed center positions. Analyzing the received data yield a mean numerical aperture $\overline{NA} = 0.91 \pm 0.05$ by a standard deviation of $\sigma_{NA} < 0.4 \cdot 10^{-3}$ and a Strehl ratio $\overline{S} = 1.02 \pm 0.10$ with $\sigma_S = 2.7 \cdot 10^{-3}$. Hence the resolution is $R = 570^{+29}_{-27}\,\text{nm}$. The small standard deviations indicate that the analysis software does not rely on the peak position of the intensity distribution. Small differences of the calculated value of the numerical aperture to the designed value can be explained by the discretization of the continuous Airy function into pixel. This is equivalent to a loss of information. ΔS is due to its direct connection to NA strongly depending on an exact determination of the position of the first minimum. The radial intensity distribution of a modeled detector signal and the relevant fits needed for the analysis are presented in Fig.5.6. For comparison a perfect Airy pattern is depicted in the same figure.

The modulation transfer function of the modeled detector signal is compared to the one of a perfect Airy pattern, see Fig.5.6.b). Both graphs are consistent with each other over the whole spatial frequency range. Since there is no general convention a cut-off frequency may be defined as the frequency where the amplitude drops below 0.1. In Fig.5.6.b) the cut-off frequency

is at approximately $1708\,\text{cycles/mm}$. This corresponds to a resolution of $R = 585\,\text{nm}$ and is in good agreement with the one out of the PSF analysis.

5.2.5. Defocussing Analysis

A perfect Airy pattern can only be expected as measured signal, if both the object and image plane are in the corresponding focal points. Finding this point in the laboratory is a non-trivial task due to the small focal depth $\Delta f < 0.8\,\mu\text{m}$ of the microscope.The data obtained by the method described in Sec.5.1.1 can be used to realize an iterative procedure to reach the optimal working point. In a first step the current defocus is determined by a single detector picture.

To do so the modeled intensity distribution of Sec.5.2.4 was transferred into the radial intensity distribution as presented in Sec.5.2.1. For each object- and image-plane position the PSF calculated from the database is read into `MATLAB` and compared to the modeled detector signal. We assume that the lenses are at the position where the calculated and measured PSF differ least. To quantify the similarity of the measured and simulated signal the following figure of merit (FoM) is used.

$$\text{Deviation} = \int |I_{\text{meas}}(r) - I_{\text{calc}}(r)| dr \tag{5.4}$$

Where the function $I_{\text{meas}}(r)$ is normalized in a way that $I_{\text{meas}}(0) = I_{\text{calc}}(0)$.

For the modeled camera signal of a perfect Airy pattern in Fig.5.7 the relevant graphs are shown. The deviation for this particular signal in dependence of image and object position is presented in a). White markers highlight the position of the minimal and maximal value of the figure of merit. In b) the measured PSF as well as the one which was calculated to have the minimal deviation are depicted. Only a minimal difference between the two PSF is visible. For comparison in c) the modeled PSF with the biggest deviation, which differs dramatically from the measured one, is shown.

Already a change of the figure of merit by 0.2 (arb. U.) causes visible deviations of the measured and expected PSF. Hence the accuracy of setting the object position with this is approximately $2\,\mu\text{m}$. The position of the image plane is determined with a precision of $2 - 3\,\text{mm}$, which is smaller then the typical measurement precision of a ruler for a distance of $\sim 2\,\text{m}$.

The knowledge on the defocus can be used to find the optimal working point iteratively. For a circular symmetric signal the following procedure describes the required steps to focus the optical system:

1: An image is measured by the camera and evaluated with the `MATLAB`-script: As a result the actual distance between lens_2 and camera as well as the distance to the optimal camera position are displayed.

2: The position of the camera is changed by the calculated distance.

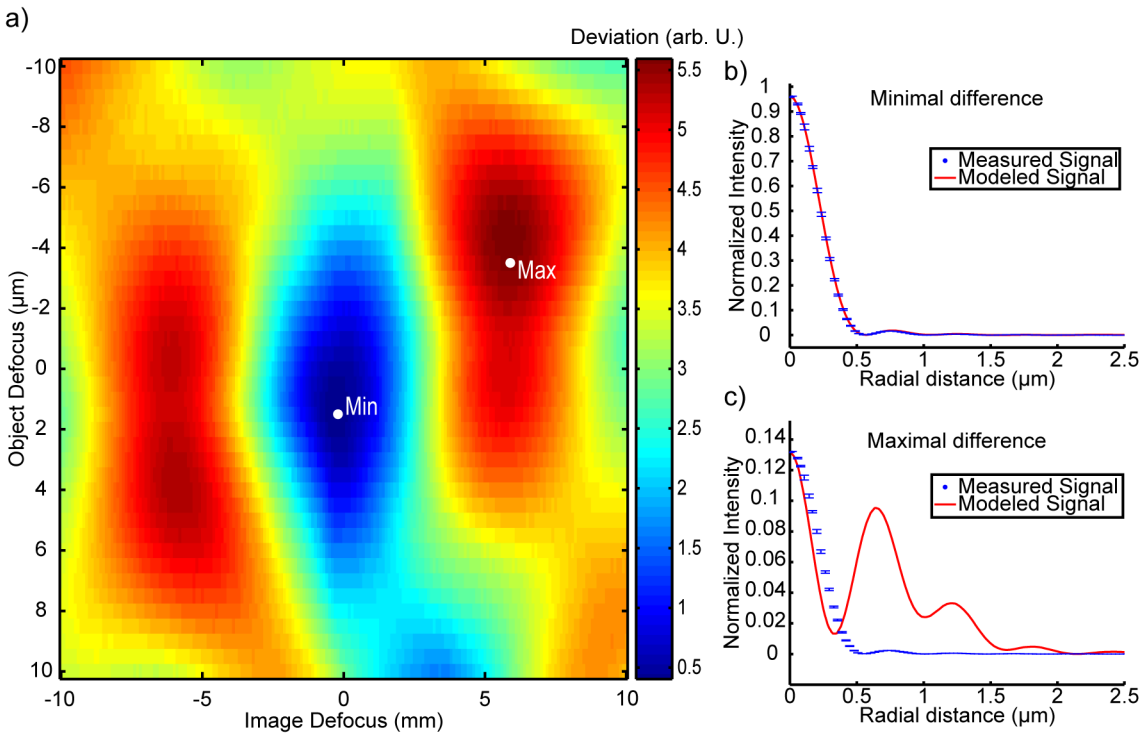

Figure 5.7.: a) Shows the value of the figure of merit for a perfect Airy disk. Inserts b) shows a clear agreement for the ideal case of no defocus. As expected for a defocussing of objective and imaging lens the accordance in insert c) is negligible.

3: The position of the object (here: SNOM-fiber) is changed to refocus the signal on the camera.

4: An almost perfect Airy pattern is reached by repeating steps 1-3.

Due to a delivery bottleneck of the SNOM-fiber tips the procedure has not been fully tested yet. But applying the defocus analysis on already measured data show consistent results, see Ch.6.

6. Characterization of a high NA Objective

The previous chapter explains how to extract information on the numerical aperture, Strehl ratio and possible misalignment of a measured signal. A demonstration of the analysis procedure was done with a simulated perfect camera image. This chapter focuses on the analysis of the data measured by imaging of a SNOM-fiber tip, see Sec.4.2.3.

6.1. Numerical aperture and Strehl intensity

In Fig.6.1 the detector signal and the radial PSF of the until now best measured signal are presented. For this measurement a lens_2 with a focal length of $f = 750\,\text{mm}$ with a magnification of $M \approx 64\times$ was used.

Applying the self-written analysis program introduced in Sec.5.2.2 to the measured signal we obtain $\text{NA}_{\text{meas}} = 0.91 \pm 0.08$ and $S_{\text{meas}} = 0.43 \pm 0.07$. Converting the NA into resolution according to Eq.2.16 yields $R_{\text{meas}} = 572^{+56}_{-47}\,\text{nm}$, which is sufficient to resolve single atoms within the planned spin-dependent optical lattice with single lattice site resolution. The measured Strehl intensity is below the diffraction limit of $S = 0.8$. In comparison to the error obtained in Sec.5.2.4 the uncertainty is increased by a factor of $2\times$. This is due to small asymmetries and the noise of the CCD-camera which increase the intensity uncertainty of each bin and hence the overall uncertainty.

The Strehl ratio of 0.4 denotes a significant amount of aberrations and a loss of contrast. Besides spherical aberration we can exclude for all kind aberrations due to the good circular symmetry of the measured signal. Spherical aberration have the origin in an imperfect lens or a defocus of the object. Therefore the defocus analysis was applied to the measured data.

The deviation between expected data and measured intensity distribution is depicted in Fig.6.2. A minimal deviation is calculated at a defocus of the object by $9.5 \pm 2\,\mu\text{m}$ with an deviation $\text{FoM} = 0.5(\text{arb. U.})$. At this position a Strehl ratio of 0.43 and $\text{NA} = 0.91$ are expected. In Fig.6.2 an additional region with a small deviation of $\text{FoM} = 0.9(\text{arb. U.})$ is located at an object defocus of $-5\,\mu\text{m}$. The analysis presented in Sec.6.3 excludes that the system is in this state and confirms that we consider the correct modeled signal.

The results of both analysis method agree well within the uncertainty region. A numerical aperture of $\text{NA} = 0.9$ is hence confirmed by this two independent analysis procedures. The new experiment in the Institute of applied Physics in Bonn will therefore feature the state of the art microscope for the observation of single atoms. The result of the defocus analysis strongly indicate that a perfectly aligned imaging system is working in the diffraction limited regime.

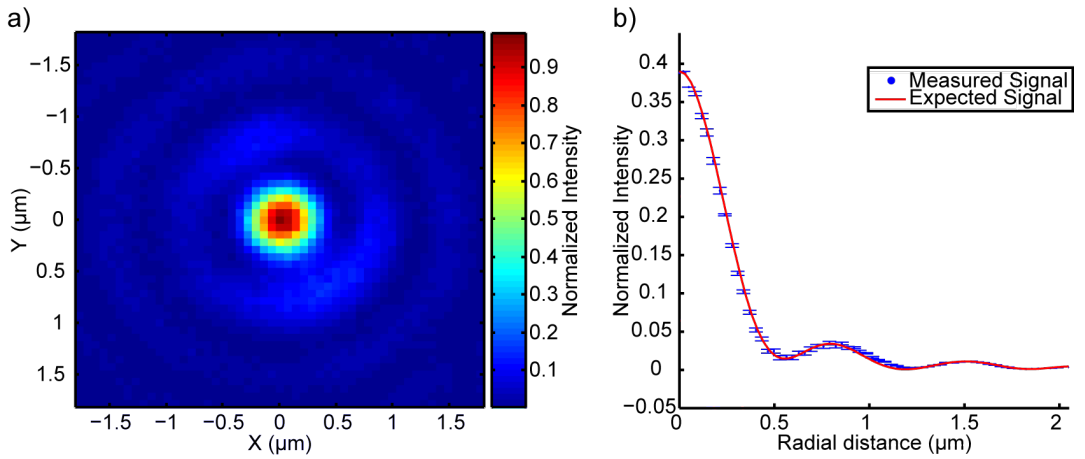

Figure 6.1.: a) Measured detector signal for the best aligned optical imaging system. b) Radial intensity distribution of the measured signal shown in a) normalized to a perfect Airy disk. Additionally the modeled PSF which divers least is shown (red).

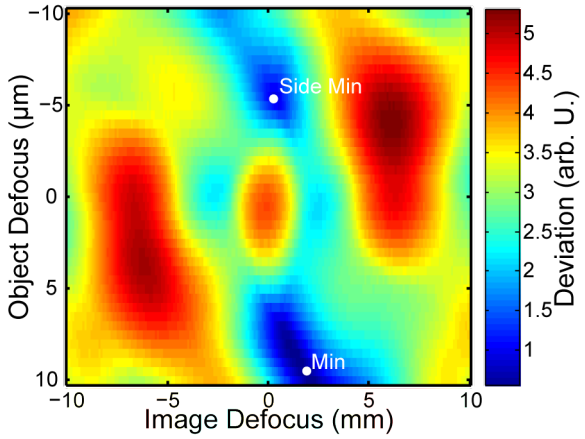

Figure 6.2.: The deviation between a single measured camera signal to the expected intensity distribution in dependence of the defocussing. The global minimum is located at an object defocus of $9.5\,\mu m$ and a side minimum is observed at an object defocus of $-5\,\mu m$.

Unfortunately is was not possible within the work for this thesis to use the procedure explained in Sec.5.2.5 to achieve a better Strehl ratio.

6.2. Modulation Transfer Function

For the same CCD-camera signal as in Sec.6.1 the modulation-transfer-function and phase-transfer-function are analyzed. To calculate those the script described in Sec.5.2.3 are used. The MTF and PTF of the measured and the modeled point-spread-function are shown in Fig.6.3.a)-b).

The agreement of the measured and modeled MTF is remarkable. Both functions show an almost linear decrease of the MTF-amplitude. An amplitude of 0.1 is reached at a spa-

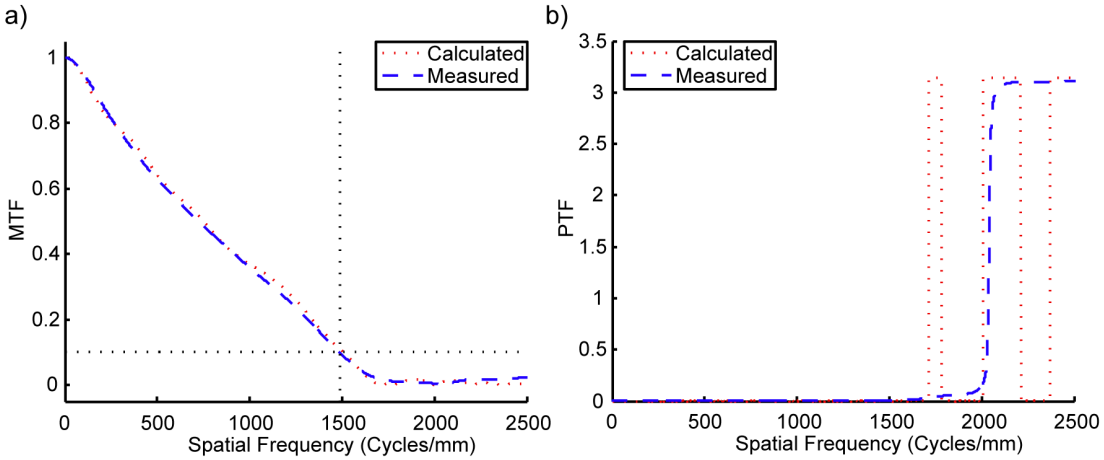

Figure 6.3.: a) Modulation transfer function for the measured signal and the PSF signal with the smallest deviations to the measured signal. The black dotted lines mark the position where the amplitude of the MTF drops below 0.1. b) The corresponding phase transfer function show no indications of phase distortions.

tial frequency of approximately $\xi = 1500\,\text{Cycles/mm}$. Using this criterion a resolution of $R = 666\,\text{nm}$ corresponding to a numerical aperture $\text{NA} = 0.78$ is obtained. The zero amplitude is reached at $\xi = 1730\,\text{Cycles/mm}$. Hence by the second possible definition a resolution of $578\,\text{nm}$ and a numerical aperture $\text{NA} = 0.89$ is achieved. Comparing this results with the value $\text{NA} = 0.91 \pm 0.06$ out of the analysis in Sec.6.1 shows a good agreement between the different evaluation methods.

The phase transfer functions are presented in Fig.6.3.b). For the measured and modeled PTF the amplitude is zero for frequencies up to $\xi = 1700$. This indicates that there are no major phase distortions. Phase jumps of π occur at higher frequencies but they are regarded as numerical artefacts since the modulation transfer function already dropped to zero.

6.3. Spherical aberration analysis

A efficient possibility to check for spherical aberration is a scan of the image plane through the focus of lens_2. A symmetric signal around the focus in the axial plane is expected as indicated in Sec.5.1.1 for a system free of spherical aberration. Distinct misalignment induced spherical aberration are expected since our analysis in Sec.6.1 showed that our object was not placed in the focus of the objective but $9.5\,\mu\text{m}$ away from it. Furthermore the analysis can be used to exclude that the system is in the state described as side minimum in Fig.6.2.

Since the asymmetries of the signal increase for a displaced image plane only cuts through the maximum in x- and y-direction of the sensor were used as PSF signal. In Fig.6.5 the measured intensity distribution for an image plane defocus of $\Delta z = -5\,\text{mm}$ and $\Delta z = +5\,\text{mm}$, including the defined axis are presented. The choice of the axis is arbitrary but the overall

behaviour of the axial intensity distribution is well described by this method. For the measurement of the axial intensity distribution the CCD-camera was scanned through the focus of lens_2 in a range of $d = f \pm 5\,\text{mm}$ for a fixed object position. Every millimeter $\Delta d = 1\,\text{mm}$ a picture of the PSF was taken to compare it with the modeled signal of the `OSLO`-program. In Fig.6.4.a) and b) the measured axial intensity distribution is shown for both axis. As expected the signals are not symmetric around the optimal image position due to the spherical aberration. The first order side maximum almost vanishes for image plane positions closer to lens_2 (negative defocus), while the center peak increases in width. Hence the resolution and Strehl ratio are decreased. For increased distances to lens_2 the width of the center peak is decreased but at the same time the intensity of the higher order side peaks is increased dramatically, which equivalent to a loss of contrast.

For comparison the expected axial intensity distribution of a by $9.5\,\mu\text{m}$ defocused object is presented in Fig.6.4.c). The overall behavior of the modeled and measured axial intensity distribution are in good agreement. In Fig.6.4.d) the intensity distribution at position of the side minimum ($d = -5\,\mu\text{m}$) in the FoM of Sec.6.1 is shown. The intensity distribution is non consistent with the measured signal and it is excluded that the system is in this state.

These results are another indication that the analysis of Sec.5.2.5 is working properly since the observed signal is similar to the expected one for the calculated defocus. At the same time the good agreement between measured and calculated signals denote a properly working imaging system.

6.4. NA in dependence of the Aperture

The theory in Ch.2 showed the dependence of the numerical aperture from the angle of divergence. A reduction of the free aperture tunes the divergence angle of the imaging system and is used to determine the characteristic curve of the NA in dependence of the free aperture.

In the later experiment a motorized iris will be implemented, which enables us to tune the values S and NA by artificially decreasing the aperture diameter. In this way the number of pixels of the EMCCD-camera (Andor XION) illuminated by a single atom can be adjusted to the optimal working point. This camera has a pixel size of $16 \times 16\,\mu\text{m}^2$ and we aim for a image size of a single atom of 3×3 pixel.

As shown in Sec.2.2 a reduction of the aperture involves a reduction of the NA since the angle of convergence is decreased. On the other hand a reduced aperture is equivalent cutting off the parts of the beam which produce the largest aberration and therefore an increase of the Strehl ratio.

A manual iris was implemented to characterize the above described behavior. The aperture diameter was decreased in steps of $2.5\,\text{mm}$ and radial intensity distribution measured. For the analysis the numerical aperture and Strehl intensity is calculated in dependence of the aperture by the scripts presented in Sec.5.2. In Fig.6.6.a)-b) these values are presented together with

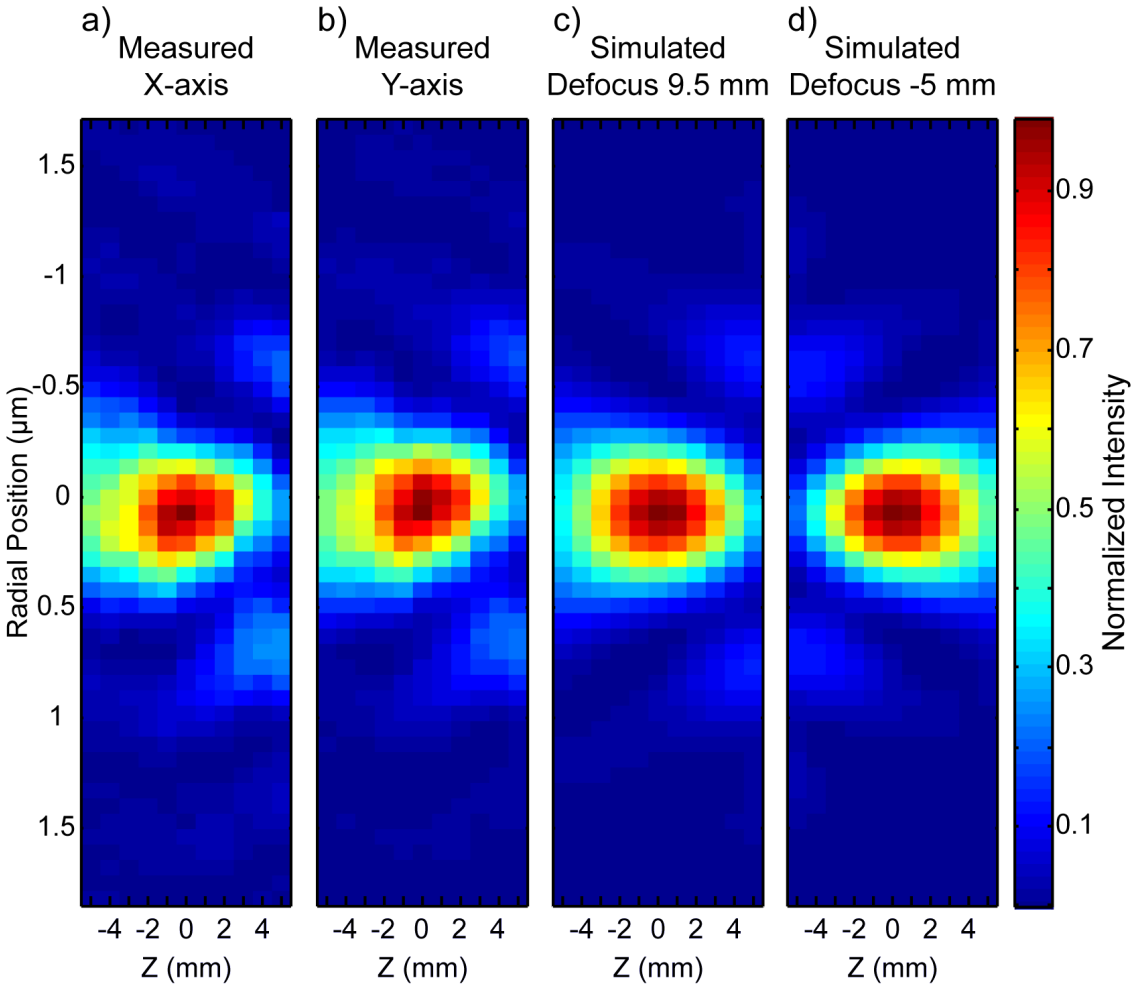

Figure 6.4.: Axial intensity distribution along a) the x-axis and b) the y-axis normalized to the corresponding peak intensity. Since the modeled signal is perfectly circular symmetric axial intensity distribution is shown along a single arbitrary chosen axis for an object defocus of c) $9.5\,\mu m$ and d) $-5\,\mu m$.

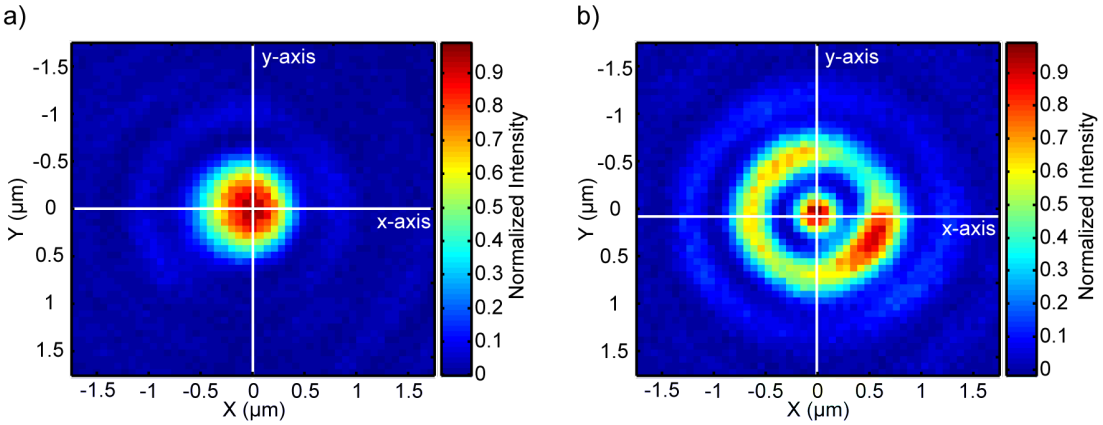

Figure 6.5.: PSF at a defocus of the image plane by a) $\Delta z = -5\,\text{mm}$ and b) $\Delta z = +5\,\text{mm}$ normalized to the corresponding peak intensity. In a) the peak intensity is in the order of $45\,\%$ of the focused image and $30\,\%$ in b). The white lines mark the axes considered for the analysis.

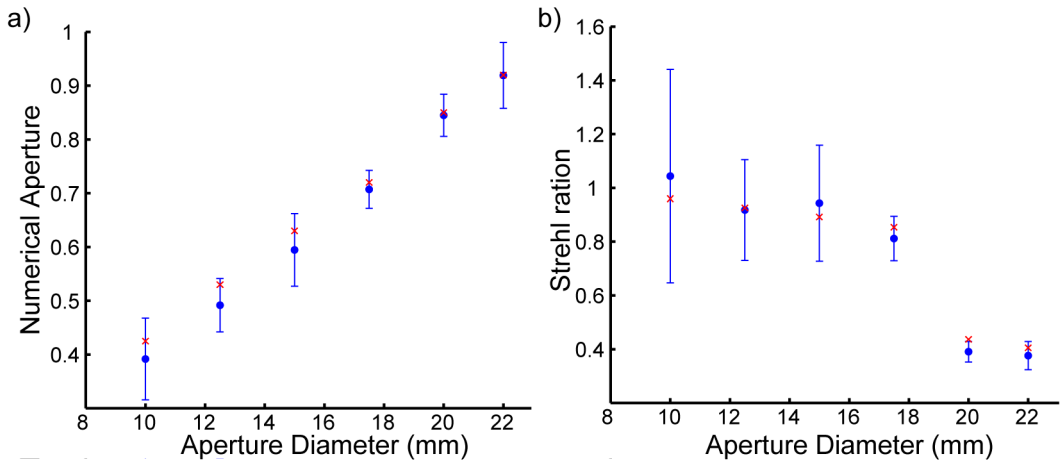

Figure 6.6.: a) Numerical aperture and b) Strehl ratio in dependence of the free aperture. Red crosses mark the modeled value. Measured values with errorbar are presented in blue.

the values expected from the model. To obtain the modeled data first the defocus of the full aperture signal was calculated to be $\Delta d_{\text{object}} = 10\,\mu\text{m}$. On the basis of this value the NA and S were calculated by the OSLO-program (see red crosses in Fig.6.6).

For all apertures the measured and expected numerical aperture values agree well within the uncertainty region. According to Eq.2.12 the almost linear increase of the NA with the aperture diameter is expected. An object defocus of $\Delta d_{\text{object}} \approx 10\,\mu\text{m}$ is not expected to change the numerical aperture dramatically since the effective focal length is $\text{EFL} = 12\,\text{mm}$. This corresponds to a relative change of the EFL by less then $0.1\,\%$.

Also the measured Strehl ratio value agree well with the modeled ones within the uncertainty region. The large error on the Strehl ratio for small aperture values originate from the strongly decreased intensity. For an aperture of $10\,\text{mm}$ diameter the peak intensity drops below $10\,\%$ of the full aperture value. The background noise of the CCD-camera stays on the same level and the relative error is increased. The Strehl ratio stays around unity for aperture diameters below $17.5\,\text{mm}$ which corresponds to a numerical aperture of $\text{NA} \approx 0.7$. For $\text{NA} \geq 0.7$ one is speaking of large numerical apertures where aberrations become distinct[14]. Larger diameters (higher NA) cause a sudden decrease to an almost constant level of the Strehl ratio $S \approx 0.4$. The defocus of the object produces spherical aberration which become significant for large convergence angle. Another equivalent interpretation is the increasing focal depth for smaller NA which shift the object into the focal region.

7. Summary and Outlook

During this thesis two state of the art high numerical aperture objective for the observation of single atoms were assembled in the clean-rooms of the CAESAR-institute in Bonn.

For the characterization of the objective several approaches were followed. A wavefront analysis of a retroreflected beam using a Shearing-interferometer resulted in first qualitative indications of a properly working imaging system.

Quantitative information on the objective were extracted by imaging of sub-micrometer-scale light sources. The production and implementation of the light-sources turned out to be extremely sensitive against all kind of environmental influences. Most significant results were obtained by imaging of aluminium coated SNOM-fiber tips onto a beam-profile-camera.

By means of a self-written analysis software a numerical aperture of NA $= 0.91 \pm 0.08$ was confirmed. The observed signal with a Strehl ratio of approximately 0.4 is not diffraction limited. However strong indications for a diffraction limited working objective were obtained by the comparison of measured signals with numerically calculated intensity distributions using the ray tracing software OSLO. Here all deviations to a perfect Airy pattern in the measured signal can conclusively attributed to spherical aberration induced by a defocus of the light-source.

The results confirm the possibility to observe atoms in our two-dimensional optical lattice with single lattice site resolution. A Strehl ratio of 0.4 leads a reduced contrast. Hence the Strehl ratio has to be increased by more precise positioning of the object to confirm the possibility of addressing atoms with single lattice site resolution.

To accomplish this an analysis routine was developed which in future will be used to estimate the defocus of the object to the quantum gas microscope out of a single camera picture. Based on this scheme an iterative alignment of the whole system will be feasible. An adoption of the analysis routine to other optical systems should be possible without much effort.

In future the set-up described in Sec.4.2.3 in combination with the analysis software out of Ch.5 will be used to proof the diffraction limitation of the quantum gas microscope. A new set of imaging lenses (LensOptics: $f = 1000\,\text{mm}$, $f = 1200\,\text{mm}$ and $f = 1500\,\text{mm}$) will allow for larger magnification and hence to reduced uncertainties. In parallel to reach the long term goal, the observation of single atoms within a two-dimensional spin-dependent optical lattice, several projects are already finished or in progress.

The vacuum apparatus including a high numerical aperture objective and the low birefringence twelve sided glass cell is positioned at the final location. After the bake-out a pressure of $1 \cdot 10^{-10}$ mbar was measured which is sufficient to trap atoms within a optical lattice. Magnetic gradient coils for trapping atoms in a two-color magneto-optical-trap are adjusted to the glass

cell as well as the correction coils.

All lasers needed to create the two-color magneto-optical trap are built. The doppler-free polarization spectroscopies for frequency locking[34] and the frequency shifts for the creation of the two-color MOT are currently under alignment.

For the two-dimensional spin-dependent optical lattice a phase-detector for light polarization synthesis was designed and characterized[35]. This device represents an advancement of the work presented in [36]. For the alignment of the optical lattice to the objective the analysis software developed in this thesis will be an assistant tool.

In the end the final characterization of the quantum gas microscope will be fulfilled with single atoms. Single atoms will be a more perfect point-source then all tested objects since the emitted light is homogeneous distributed over the full solid angle.

A. Construction of a sub-micrometer scale light Source

The creation of a stable light source with an aperture below $500\,\mathrm{nm}$ is a non-trivial task. In the following the production procedures and properties of the tested light sources are summarized.

A.1. SNOM-fiber preparation

The aluminium coated SNOM-fiber tips are produced out of Nufern 780-HP fibers by mechanical pulling. Light transmitted through the tip is attenuated by a factor of approx. $1 \cdot 10^{-4}$. Considering the damage threshold of $400\,\mu\mathrm{W}$ a power in the order of several hundred nW is expected. In the following the steps needed to prepare and align the SNOM-fiber are explained shortly. Fig.A.1 illustrates the procedure.

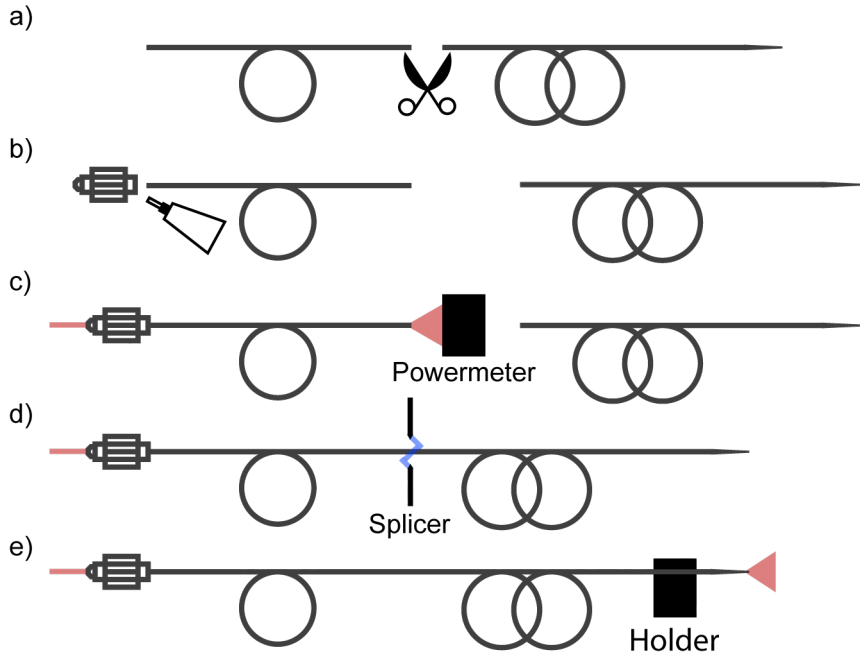

Figure A.1.: Preparation procedure of the SNOM-fiber tip as explained in the text.

The fibers are delivered without an optical connector. Hence glueing and polishing of the connector had to be done in the institute. First the fiber is into two parts. The optical connector is glued to the fiber without the tip. Light is coupled into the connector and the transmitted power measured to ensure the damage threshold of the tip is not exceeded. At the same time the amount of light emitted by the tip is maximized. Afterwards the ends of both fibers were again connected by the use of a fiber splicer (Ericsson FSU995PM).

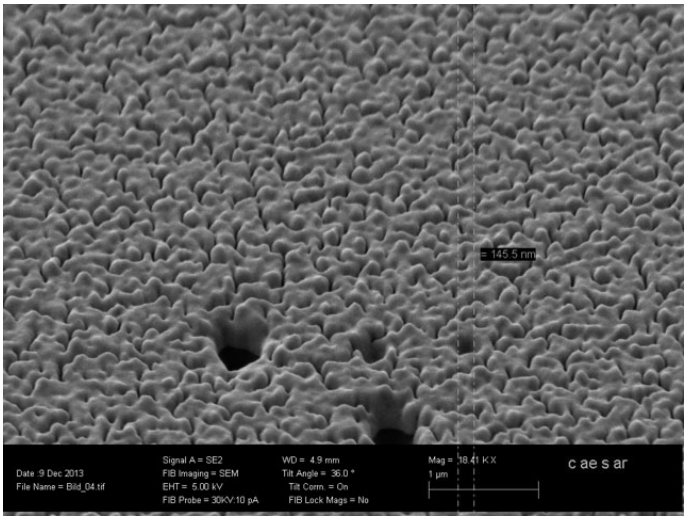

Figure A.2.: Scanning electron microscopy picture of the gold substrate evaporated on a glass microscopy plate. The surface is rough and shows a lot of mayor dips which might cause the low attenuation values. Furthermore holes drilled by the fast ion beam of diameter $320\,\text{nm}$, $220\,\text{nm}$ and $145.5\,\text{nm}$ (from left to right) are shown.

The tip was mounted on a bare fiber holder (Newport: 466A-711). The last centimeter of the fiber has no protective coating but a thin aluminium layer. Fixing of the tip was done approx. $1\,\text{cm}$ away from the tip to ensure the aluminium coating is not damaged. Finally the holder was mounted on the precision translation stage by a self-made adapter.

A.2. Production of pinholes

Commercially available pinholes have a minimal diameter of $\varnothing = 1\,\mu\text{m}$. This aperture size is an order of magnitude to large for our purposes. For the production of a sub-micrometer pinhole the substrate layer should not be to large to keep the loses small. At the same time the layer needs to exhibit a certain thickness to guarantee a sufficient attenuation factor. Hence it was decided to use thin metallic substrates placed on microscopy glass plates.

To estimate the attenuation of a laser beam due to the substrate the Beer-Lambert law is used As one of the prerequisite for the valid application of the Beer-Lambert law the attenuating medium has to be homogeneous. In Fig.A.2 a scanning electron microscope image of the metallic substrate with several test drill-holes is shown. Clearly visible are inhomogeneities leading to a reduced attenuation factor as described in Sec.4.2.1.

Acknowledgments

A year full of work, excited discussion and new experiences comes to an end. Therefore it is the time to express my gratitude towards the people who put a lot of trust in me and made my stay in the AG Meschede to such a great time.

First of all I want to thank Professor Dieter Meschede for giving me the opportunity to complete my master thesis at the construction of such a promising experiment. I will definitely observe the further development of this project with great interest.

Also I want to thank Dr. Andrea Alberti for a lot of productive discussions and a huge number of good advices. The same share goes to Dr. Wolfgang Alt for the enormous experimental knowledge he willingly shared with me.

Also I am indebted to Stefan Brakhane for supervising me and his presence during the long working days in the clean rooms of the CAESER-Institut. Especially I want to give my gratitude to Carsten Robens who designed the objective with such remarkable properties. Without his efforts this thesis would not have been come about.

Thank you.

Bibliography

[1] R. Feynman. Simulating physics with computers. *International Journal of Theoretical Physics*, 21, 1982.

[2] S. Lloyd. Universal quantum simulators. *Science*, 273, August 1996.

[3] I. Buluta and Franco Nori. Quantum simulators. *Science*, 326, October 2009.

[4] P. Walther and A. Aspuru-Guzik. Photonic quantum simulators. *Nature Physics*, 8, April 2012.

[5] A. A. Houck, H. E. Türeci, and J. Koch. On-chip quantum simulation with superconducting cricuits. *Nature Physics*, 8, April 2012.

[6] I. Bloch, J. Dalibard, and S. Nascimbene. Quantum simulations with ultracold quantum gases. *Nature Physics*, 8, April 2012.

[7] I. Bloch. Ultracold quantum gases in optical lattices. *Nature Physics*, 1, October 2005.

[8] M. Karski, L. Förster, J. Choi, W. Alt, A. Widera, and D. Meschede. Nearest-neighbor detection of atoms in a 1d optical lattice by fluorescence imaging. *Phys. Rev. Lett.*, 102:053001, 1996.

[9] J. F. Sherson, C. Weitenberg, M. Endres, M. Cheneau, I. Bloch, and S. Kuhr. Single-atom-resolved fluorescence imaging of an atomic mott insulator. *Nature*, 467, September 2010.

[10] C. Weitenberg, M. Enders, J. F. Sherson, M. Cheneau, P. Schauß, T. Fukuhara, and I. Bloch. Single-spin addressing in an atomic mott insulator. *Nature*, March 2011.

[11] M. Karski, L. Förster, J. Choi, A. Steffen, N. Belmechri, W. Alt, D. Meschede, and A. Widera. Imprinting patterns of neutral atoms in an optical lattice using magnetic resonance techniques. *New J. Phys.*, 12:065027, 1996.

[12] W. S. Bakr, J. I. Gillen, A. Peng, S. Fölling, and M. Greiner. A quantum gas microscope for detecting single atoms an a hubbard-regime optical lattice. *Nature*, 462, November 2009.

[13] M. Karski. Doktorarbeit: State-selective transport of single neutral atoms. 2010.

[14] M. Gu. *Advanced optical imaging theory*. Springer, 1999.

[15] M. Born and E. Wolf. *Principles of Optics*. Cambridge University Press, 1999.

[16] W. Zinth and U. Zinth. *Optik: Lichtstrahlen-Wellen-Photonen*. Oldenbourd, 2009.

[17] G. D. Boreman. *Modulation Transfer Function in Optical and Electro-Optical Systems*. Spie Press, 2001.

[18] W. T. Welford. *Aberrations of Optical Systems*. Adam Hilger, 1991.

[19] B. Sick, B. Hecht, U. P. Wild, and L. Novotny. Probing confined fields with single molecules and vice versa. *Journal of Microscopy*, 202, May 2001.

[20] D. Malacara and Z. Malacara. *Handbook of Optical Design, Second Edition*. Dekker, 2009.

[21] *Optisches Glas - Datenblätter*. SCHOTT, 2013.

[22] S. M. Mansfield and G. S. Kino. Solid imersion microscope. *Applied Physics Letters*, 57, October 1990.

[23] S. Yim, J. H. Kim, and J. Lee. Solid immersion lens microscope for spectroscopy of nanostructure materials. *Journal of the Optical Society of Korea*, 15, March 2011.

[24] A. Steffen, W. Alt, M. Genske, D. Meschede, C. Robens, and A. Alberti. In situ measurement of vacuum window birefringence by atomic spectroscopy. *Review Of Scientific Instruments*, 84, August 2013.

[25] *Informationszentrum Technische Keramik*. www.keramik-rs.de, 2013.

[26] Y. Golan, L. Margukis, and I. Rubinstein. Vacuum-deposited gold films: I. factors affecting the film morphology. *Surface science*, 264, October 1991.

[27] H. Schneckenburger. Total internal reflection fluorescence mircosopy. *Current Opinion in Biotechnology*, 16, February 2005.

[28] D. Axelrod. Evanescent excitation and emission in fluorescence microscopy. *Biophysical Journal*, 104, April 2013.

[29] D. Axelrod, T. P. Burghardt, and N. L. Thompson. Total internal reflection fluorescence. *Ann. Rev. Biophys. Bioen.*, 1984.

[30] L. Novotny, M. R. Beversluis, K. S. Youngworth, and T. G. Brown. Longitudinal field modes probed by single molecules. *Physical Review Letters*, 86, June 2001.

[31] A. Drezet, M. J. Nasse, S. Huant, and J. C. Woehl. The optical near-field of an aperture tip. *Europhysics Letters*, 66, April 2004.

[32] Thorlabs lens-datasheet: La1727-b.

[33] R. J. Barlow. *Statistics: A guide to the use of statistical methods in physical science*. Wiley, 2002.

[34] C. P. Pearman, C. S. Adams, S. G. Cox, P. F. Griffin, D. A. Smith, and I. G. Hughes. Polarization spectroscopy of a closed atomic transition: application to laser frequency locking. *Journal of Physics B: Atomic, Molecular and Optical Physics*, 35, 2002.

[35] S. Shestovy. Entwicklung eines hochstabilen optischen phasendetektors für licht-polarisationssynthese. September 2014.

[36] A. Hambitzer. Direct syntheis of light polarization for state-dependent transport. October 2012.

Declaration

I hereby declare that this thesis was formulated by myself and that no sources or tools other than those cited were used.

Bonn, 30.08.2014